Physics – Uspekhi **47** (3) 249 – 272 (2004)

REVIEWS OF TOPICAL PROBLEMS PACS numbers: **63.20. – e**, 63.20.Dj, **78.30. – j**

Investigation of semiconductors with defects using Raman scattering

L A Falkovsky

DOI: 10.1070/PU2004v047n03ABEH001735

Contents

Abstract. The influence of defects and carriers on lattice dynamics, especially on Raman scattering from semiconductors and metals, is considered; a comparison of the theory with experimental data is made. Phonon scattering by point, line, and plane defects produces a phonon shift and phonon broadening, which influence the Raman line shape. This effect is used for investigating strain at interfaces and for characterizing semiconductor devices. Phonon interaction with carriers involves a Coulomb field excited by optical-phonon vibrations. Our treatment of the electron – phonon interaction is based on the Born – Oppenheimer adiabatic approximation. The effect of carriers is essential near the edge of the $\omega - k$ region where Landau damping appears due to the electron – hole excitation. A possibility to determine the electron – phonon coupling constant from experiments with the phonon – plasmon coupled modes is discussed.

1. Introduction

As is well known, the main progress in the experimental investigation of phonon spectra was made with the aid of thermal neutrons many years ago. In recent years, however, extensive use has been made of inelastic X-ray scattering and Raman light scattering to attain these ends. In the latter case, the scattering is observed with laser radiation, whose wavelength is long in comparison with the lattice constant a of the crystal under investigation, and the transferred wave vector proves to be small, $q \ll 1/a$. This is the reason why the phonon frequencies in experiments on Raman scattering (RS) are determined only at the center of the Brillouin zone, $q = 0$. This limitation is compensated for by a higher (in comparison with neutrons) frequency resolution, which amounts to 1 cm^{-1}, making it possible to measure not only the position of the line, but also its structure, i.e., its width and asymmetry. The lineshape proved to be sensitive, in particular, to the presence of various defects in the sample. There emerged a new area of experimental investigations, the so-called micro-Raman spectroscopy. Stress and defect distributions in semiconductors are investigated with a high spatial resolution employing a laser beam focused to wavelength dimensions on the order of 1 μm.

The effect of homogeneous pressure or isotopic substitution on the phonon spectrum has been studied in many semiconductors. The corresponding phonon frequency shift is readily explicable on the basis of rather simple notions of lattice dynamics. Explaining the broadening and asymmetry of Raman lines requires invoking the quantum-mechanical scattering theory. In this case, account should be taken of the interaction of different branches of the vibrational spectrum corresponding, for instance, to propagating and localized modes. Furthermore, the presence of defects is quite often responsible for the emergence of charge carriers. Thus, we are led to the necessity of analyzing the effect of electron – phonon interaction on the phonon spectrum of heavily doped semiconductors and metals.

The application of Raman spectroscopy to the study of semiconductors is the subject of a wealth of papers. However, experimenters have traditionally recorded only the line positions and have disregarded width and asymmetry. So far, works wherein investigations have been made of the line shapes are scarce, and we would like to bring to the attention of the reader precisely this aspect of Raman spectroscopy. The aim of our review is to outline the presently existing

L A Falkovsky L D Landau Institute for Theoretical Physics, Russian Academy of Sciences, ul. Kosygina 2, 119334 Moscow, Russian Federation
Tel. (7-095) 137 32 44. Fax (7-095) 938 20 77
E-mail: falk@itp.ac.ru

Received 1 September 2003
Uspekhi Fizicheskikh Nauk **174** (3) 259 – 283 (2004)
Translated by E N Ragozin; edited by M V Chekhova

notions of the effect of different factors on phonon damping or, more precisely, on the linewidth of inelastic single-phonon scattering.

2. Dispersion and width of optical phonons. Qualitative estimates

Bearing in mind the application of Raman spectroscopy to the investigation of disorder, we give an estimate of the spectral parameters for optical phonons, as well as the constants for their interaction with each other and with various defects. In RS experiments, measurements are made of the phonon frequency $\omega(\mathbf{q})$ corresponding to the transferred momentum $\mathbf{q}$. As already noted, this momentum is small in comparison with the size of the Brillouin zone, and so we will make use of the expansion of the phonon spectrum about the zone center,

$$\omega^2(\mathbf{q}) = \omega_0^2 \pm s^2 q^2 - \mathrm{i}\omega\Gamma\,, \tag{1}$$

where the $(+)$ sign corresponds to the branch minimum and the $(-)$ sign to the maximum. The dependence of dispersion parameter s on the direction $\mathbf{q}$ is of no great importance to us; what matters are the orders of magnitude for s, the limiting frequency ω_0, and the phonon width Γ. To estimate them, we write the phonon Hamiltonian in the symbolic form

$$H \simeq -\frac{M\omega^2 u^2}{2} + \frac{\varepsilon_0}{a^2}\,u^2(1 \pm a^2 q^2) + \frac{\varepsilon_0}{a^3}\,u^3\,. \tag{2}$$

The first term represents the kinetic vibration energy $Mv^2/2$ per atom. The second term is the potential energy in the harmonic approximation, i.e., written to the second order in the displacement u. This term is also expanded in qa, where a is the lattice constant. The factor ε_0/a^2 is the second derivative of the Coulomb interaction energy ε_0 for two atoms separated by the distance a. This energy is on the order of $\varepsilon_0 \sim e^2/a \sim \hbar^2/ma^2 \sim 5$ eV, where the ion charge is assumed to be on the order of the electron charge and m is the electron mass. Comparing the first two terms in Eqn (2) gives the frequency ω_0 which appears in expression (1): $\omega_0^2 = \varepsilon_0/Ma^2$. We employ the estimate of ε_0 to obtain

$$\omega_0 \sim \varepsilon_0\sqrt{\frac{m}{M}}\,, \qquad s \sim v\sqrt{\frac{m}{M}}\,, \tag{3}$$

where $v = \hbar/am \sim 10^8$ cm s^{-1} is the velocity of valence electrons in dielectrics or conduction electrons in metals. For the middle of the Periodic system, $M/m \sim 10^5$ and we obtain $\omega_0 \sim 3 \times 10^2$ K and $s \sim 3 \times 10^5$ cm s^{-1}. Note that the dispersion parameter s for optical phonons is on the order of the sound velocity in a solid.

The last term in Eqn (2) is a third-order term in the displacement u; it describes the transformation of one phonon to two other phonons, which is nearly always possible for optical phonons even at a zero temperature. These anharmonic processes underlie the so-called natural phonon linewidth Γ^{nat}. Since the relative magnitude of anharmonic terms is u/a, in the second order of the quantum-mechanical perturbation theory we obtain $\Gamma^{\mathrm{nat}}/\omega_0 \sim (u/a)^2$. To estimate the displacement u, we write down the vibration energy per atom,

$$M\omega_0^2 u^2 \sim \hbar\omega_0\left(n + \frac{1}{2}\right),$$

where the mean number of phonons $n \ll 1$ when the temperature is low ($T \ll \omega_0$) and $n = T/\omega$ for high temperatures ($T \gg \omega_0$). Therefore, with the use of Eqn (3) we obtain, for instance, for low temperatures

$$u^2 \sim a^2\sqrt{\frac{m}{M}}\,, \qquad \Gamma^{\mathrm{nat}} \sim \omega_0\sqrt{\frac{m}{M}}\,. \tag{4}$$

Despite the low value of the parameter $\sqrt{m/M} \sim 10^{-2}$, the processes of phonon decay result in the linewidth Γ^{nat}, which manifests itself in Raman spectra, as well as in the finite mean free path of the optical phonons r_γ. The latter can be estimated from Eqn (1) by substituting r_γ for $1/q$: $(s/r_\gamma)^2 \sim \omega\Gamma$. We obtain

$$r_\gamma \sim a\sqrt{\frac{\omega_0}{\Gamma^{\mathrm{nat}}}} \sim 10a.$$

The cross section for anharmonic processes exhibits a rather weak temperature dependence, since there exists no singularity in the final density of states for these processes. That is why the natural width Γ^{nat} can be assumed, up to room temperature, to be independent of both the temperature (its temperature dependence is given, for instance, in Refs [1, 2]) and the frequency in a sufficiently narrow frequency interval with a width on the order of Γ^{nat} in the neighborhood of the ω_0 spectral line peak, which is of interest when investigating the dependence of the width on different factors. In experiments this line has a Lorentzian shape.

However, a certain number of defects are always inherent in a real crystal. Isotopic defects are the simplest example of such disorder. Their effect on the density of states of vibrational spectra was discussed in reviews [3–6] and on Raman spectra, for instance, in Ref. [7]. In the general case, the influence of defects on the phonon spectrum reduces to the fluctuations of the deformation they produce. Figure 1 shows schematically the stress distribution near the surface of a semiconductor or its interface with a different material. If the stress were homogeneous (the straight line a), the problem would reduce to the well-known problem [8–14] of the effect of pressure on the phonon spectrum. In our case it is possible to introduce a coordinate-dependent deformation tensor $\varepsilon_{lm}(\mathbf{r})$ and write the variation of coupling constants as the

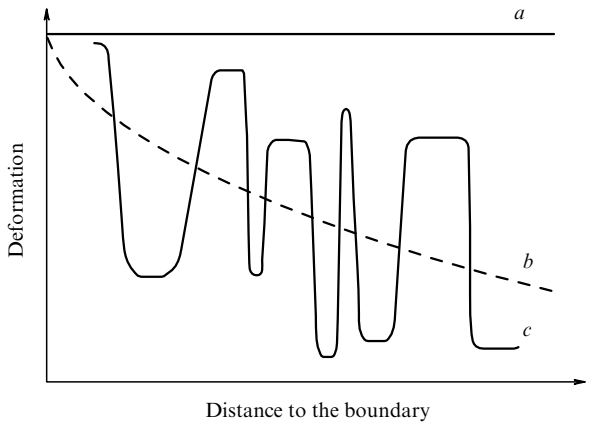

Figure 1. Schematic deformation distribution near the semiconductor boundary. Shown is the deformation (b), which dies out with depth in the sample, as well as the fluctuating component (c). The straight line (a) corresponds to a homogeneous stress in the sample under pressure.

first expansion term

$$V_{ij}(\mathbf{r}) = \sum_{lm} \lambda_{ijlm}\varepsilon_{lm}(\mathbf{r}) , \quad (5)$$

where the subscript i labels degenerate or close phonon branches.

On the other hand, the effect of disorder is conveniently represented as the resultant action of defects localized at point $\mathbf{r}_n$:

$$V_{ij}(\mathbf{r}) = \sum_n v_{ij}(\mathbf{r} - \mathbf{r}_n) = \sum_{n,\mathbf{q}} v_{ij}(\mathbf{q}) \exp\left[i\mathbf{q}(\mathbf{r} - \mathbf{r}_n)\right] . \quad (6)$$

For finite dimensions of the laser-irradiated spot, the result should be averaged over the location of defects residing within this spot. Smooth variation of the phonon frequencies at distances exceeding the spot size is retained on such averaging. In the first order in the V_{ij} interaction, we arrive at a secular equation whose rank is defined by the number of degenerate branches and the coefficients are given by the mean values of the interaction constants. In the case of a single branch, for instance, the phonon frequency shift is

$$\omega^2 - \omega^2(\mathbf{q}) = \langle V(\mathbf{r}) \rangle = cv(\mathbf{q} = 0) , \quad (7)$$

where c is the volume density of defects. For linear (or planar) defects, $v(\mathbf{q})$ depends on the two-dimensional (or one-dimensional) vector $\mathbf{q}$, and therefore the density of defects is calculated per unit area (or length). Note that the spectral parameter in all of our formulas is written as ω^2, because this is precisely how it appears in the effective Hamiltonian (2).

Expression (7) gives the phonon frequency shift arising from the variation of the medium field but tells nothing about the broadening. The reason for the experimentally observed broadening is sometimes referred to [15] as 'the relaxation of momentum conservation law'. It is estimated [16, 17] by forming the convolution of the Lorentzian line profile with some Raman frequency shift distribution arising from the local stress. As is easy to see, too great a stress variation is required to account for the observed broadening in that way. We note, however, that the ordinary phonon scattering by defects should lead to phonon damping and the corresponding broadening of the Raman spectrum.

Indeed, in the second order of the perturbation theory we obtain [18]:

$$\Gamma(\mathbf{k}, \omega) - \Gamma^{\text{nat}} \sim c \sum_{\mathbf{q}} \left|v(\mathbf{q} - \mathbf{k})\right|^2 \delta\left[\omega^2(\mathbf{q}) - \omega^2\right] , \quad (8)$$

where $\mathbf{k}$ and ω are the initial momentum and frequency of the phonon, while $\mathbf{q}$ and $\omega(\mathbf{q})$ are the momentum and frequency in the final state; the Dirac δ function ensures the energy conservation in the phonon scattering by the static disorder.

For frequencies $|\omega - \omega_0| \sim \Gamma$ near the center of the Raman line, only the range $q_\Gamma \sim \sqrt{\omega_0\Gamma}/s \sim \sqrt{\Gamma/\omega_0}/a$ is of significance in the integration in Eqn (8). Because of this, the result depends on the ratio between the range r_v of the interaction potential $v(\mathbf{r})$ and $1/q_\Gamma$. Clearly, the elastic stress about an uncharged defect decays primarily at an interatomic distance, i.e., $r_v \sim a$. For such defects, $r_v q_\Gamma < 1$, i.e., they are short-range. In this case, the matrix element can be taken to be a constant $v(\mathbf{q} \to 0) = v_0$. Isotopic defects are known to be short-range, and for them the potential is $v_0 = (1 - M/M_0)a^3\omega^2$, where M and M_0 are the respective masses of the defect and the matrix atom. For point defects, the summation (integration) in Eqn (8) is performed with respect to the three-dimensional vectors $\mathbf{q}$. Therefore, the scattering of phonons from the neighborhood of the maximum of the optical branch by isotopic defects leads to their width

$$\Gamma(\mathbf{k}, \omega) - \Gamma^{\text{nat}} = c\left(1 - \frac{M}{M_0}\right)^2 \left(\frac{a^2\omega_0}{s}\right)^3 \sqrt{\omega_0^2 - \omega^2} . \quad (9)$$

For linear defects, e.g., dislocations, the summation in Eqn (8) is performed over the two-dimensional vectors $\mathbf{q}$ and for planar defects — like a planar stacking fault or a crystallite boundary — with respect to the one-dimensional vectors $\mathbf{q}$. Therefore, the contribution of defects to the linewidth depends strongly on the density of the final phonon states: it is proportional to $(\omega_0 - \omega)^{1/2}$ for the scattering by point defects, contains a jump $\theta(\omega_0 - \omega)$ for linear defects, and diverges as $(\omega_0 - \omega)^{-1/2}$ for planar defects. Unlike the natural width, the defect-induced broadening manifests itself only for frequencies $\omega < \omega_0$, where the final phonon states occur. Recall that we are dealing now with the neighborhood of the maximum of the phonon branch. Where the phonon branch has a minimum, there emerges an additional contribution to the broadening on the high-frequency side $\omega > \omega_0$. One can see that the lineshape as a function of the transferred frequency proves to be asymmetric.

Figure 2 from Ref. [19] shows the Raman spectra of transverse optical (TO) phonons of isotopically modified ZnSe. The high-frequency wing decays more slowly than the low-frequency one. This shows up most clearly, for instance,

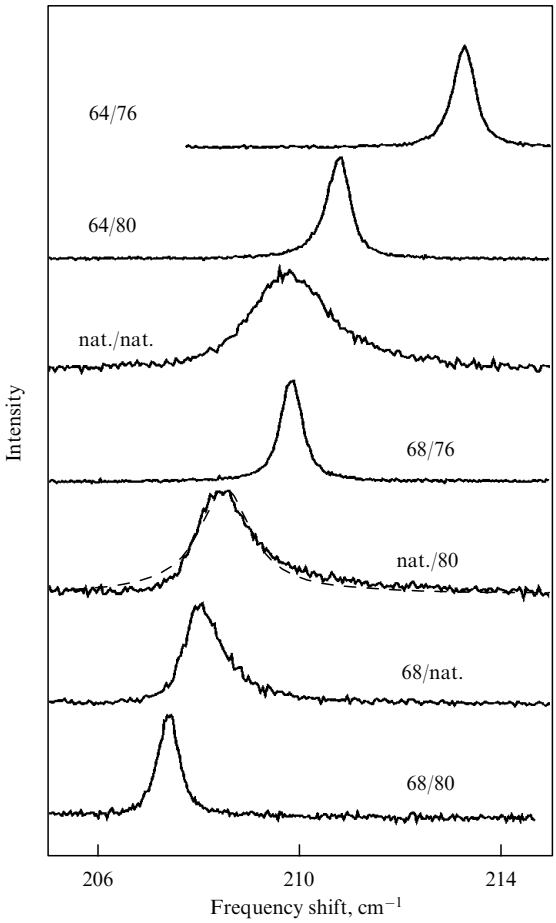

Figure 2. Raman spectra of TO phonons of isotopically substituted ZnSe, from Ref. [19].

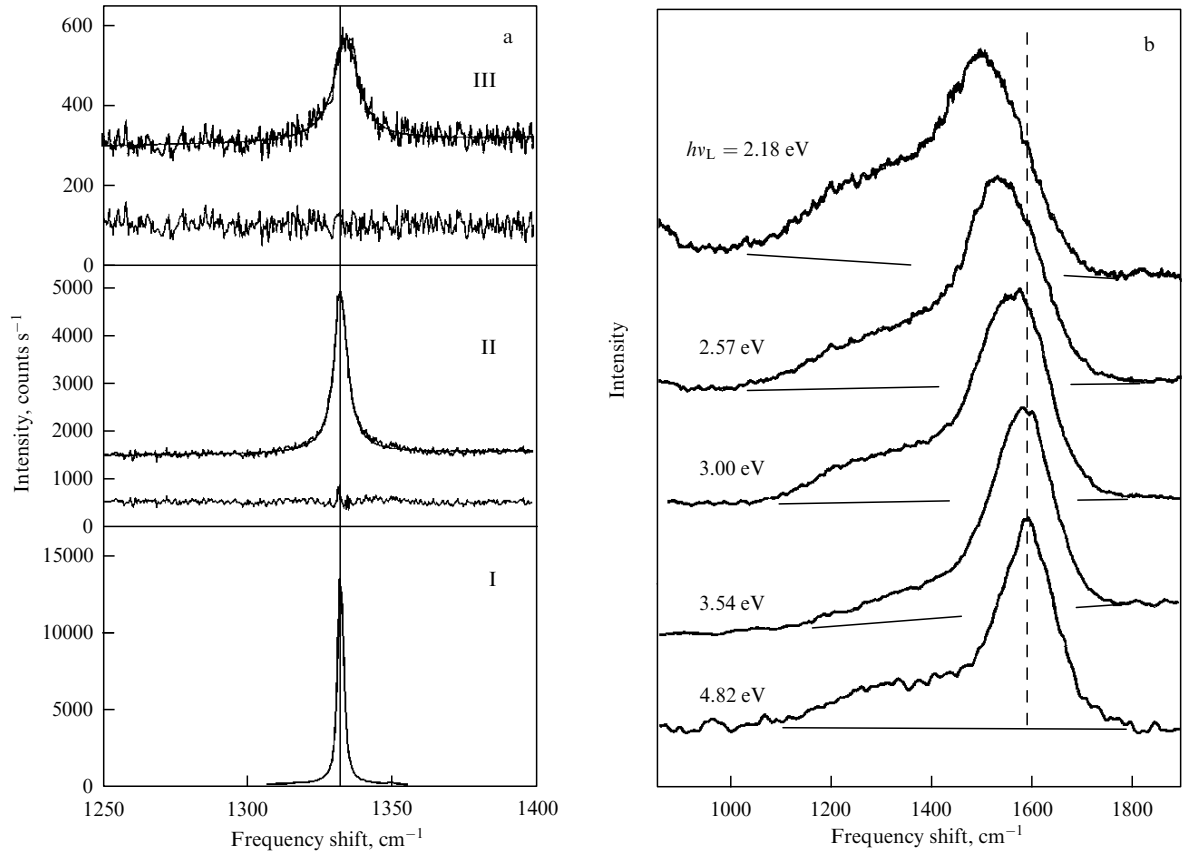

Figure 3. (a) 1330-cm^{-1} line of Raman scattering from a crystal diamond film [diamond (I), high-quality film (II), film with a relatively low quality (III)] from Ref. [20]; (b) 1500-cm^{-1} Raman line of a graphite-like material (carbon deposited in the atmosphere of hydrogen) from Ref. [21].

in a sample with a natural isotopic zinc composition and ^{80}Se. This asymmetry indicates conclusively that the TO phonon branch in ZnSe has a minimum at the center of the Brillouin zone.

It is interesting to compare (Fig. 3) the profile of the 1330-cm^{-1} line from a crystal diamond film from Ref. [20] with the 1500-cm^{-1} line from a graphite-like material from Ref. [21]. In Fig. 3a, the high-frequency wing slopes the most gently, while in Fig. 3b it is the low-frequency one. The maximum for the corresponding optical branch in graphite is a well-established fact and the existence of the minimum for diamond [22] is presently being debated. Figure 4 shows the results of one such calculation. The Raman spectra are an argument in favor of the existence of the minimum.

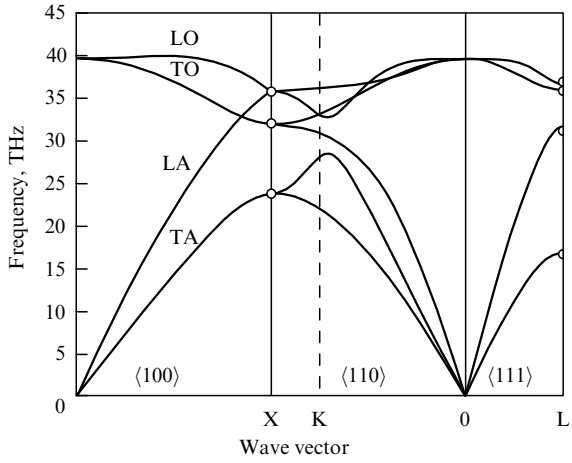

Figure 4. Phonon spectrum of diamond with a minimum for one of the branches at the Brillouin zone center. LA and TA, LO and TO are the spectra of longitudinal and transverse acoustic and optical phonons, respectively.

One can see that the spectral line profile depends on the geometry of defects inherent in the sample. However, formula (8) by itself is unsuitable for the quantitative description of the effect of defects on RS: for $\omega \to \omega_0$, the result turns to zero for point defects but diverges for linear and planar defects. To derive a result that is also valid near the ω_0 line center, the intrinsic phonon linewidth should be taken into account.

3. Influence of defects of various geometry on Raman scattering

The results that are free from the above-noted drawbacks and simultaneously give the phonon shift and width can be obtained by resorting to the well-known Green function approach. In this case, calculations should be made of the experimentally measured Raman cross section. We introduce a Hamiltonian which describes the scattering,

$$\hat{\mathcal{H}} = \frac{e^2}{mc^2} \int \frac{\mathrm{d}^3 k^{(\mathrm{s})}\, \mathrm{d}^3 k^{(\mathrm{i})}}{(2\pi)^6}\, g_{\alpha\beta\gamma} u_\alpha(\mathbf{k}^{(\mathrm{i})} - \mathbf{k}^{(\mathrm{s})}) A_\beta(\mathbf{k}^{(\mathrm{i})}) A_\gamma(\mathbf{k}^{(\mathrm{s})})\,, \tag{10}$$

where $A_\beta(\mathbf{k}^{(\mathrm{i})})$ and $A_\gamma(\mathbf{k}^{(\mathrm{s})})$ are the respective vector potentials of the incident and scattered light and $g_{\alpha\beta\gamma}$ is the so-called RS tensor. The specific form of this tensor depends on the symmetry of the phonon representation under consideration.

Since the Hamiltonian is linear in phonon displacements $u_\alpha(\mathbf{k})$, the effective cross section of scattering into the frequency interval $\mathrm{d}\omega^{(\mathrm{s})}$ and the solid angle $\mathrm{d}\Omega^{(\mathrm{s})}$,

$$\frac{\mathrm{d}\sigma}{\mathrm{d}\omega^{(\mathrm{s})}\,\mathrm{d}\Omega^{(\mathrm{s})}} = \left(\frac{4e^2\omega^{(\mathrm{s})}}{c^2\hbar m\omega^{(\mathrm{i})}}\right)^2 \frac{g_{\alpha\beta\gamma}e^{(\mathrm{i})}_\beta e^{(\mathrm{s})}_\gamma g_{\alpha'\beta'\gamma'}e^{(\mathrm{i})}_{\beta'}e^{(\mathrm{s})}_{\gamma'}}{\pi\left[1-\exp(-\hbar\omega/k_\mathrm{B}T)\right]} \times \operatorname{Im} D_{\alpha\alpha'}(\mathbf{k},\omega)\,, \tag{11}$$

is expressed in terms of the phonon Green function $D_{\alpha\alpha'}(\mathbf{k},\omega)$, where $e^{(\mathrm{i})}_\beta$ and $e^{(\mathrm{s})}_\gamma$ are the polarization vectors of the incident and scattered light, and $\mathbf{k}=\mathbf{k}^{(\mathrm{i})}-\mathbf{k}^{(\mathrm{s})}$ and $\omega=\omega^{(\mathrm{i})}-\omega^{(\mathrm{s})}$ are the transferred momentum and frequency. For the Stokes and anti-Stokes parts of the spectrum, the frequency $\omega>0$ and $\omega<0$, respectively.

In the absence of defects, the Green function is diagonal,

$$D^{(0)}_{ii}(\mathbf{k},\omega) = \left(\omega_i^2(\mathbf{k}) - \omega^2 - \mathrm{i}\omega\Gamma^{\mathrm{nat}}\right)^{-1},$$

and we find that the ith mode contribution is Lorentzian in form. Assuming the width Γ^{nat} to be small in comparison with ω_0, we obtain, for instance, in the neighborhood of the Stokes line center, $\omega=\omega_0$,

$$\operatorname{Im} D^{(0)}_{ii}(\mathbf{k}\to 0,\omega) = \frac{\omega\Gamma^{\mathrm{nat}}}{(\omega_0^2-\omega^2)^2+(\omega\Gamma^{\mathrm{nat}})^2} = \frac{\Gamma^{\mathrm{nat}}/4}{(\omega_0-\omega)^2+(\Gamma^{\mathrm{nat}}/2)^2}\,.$$

To find the Green function in the presence of defects, one needs to solve the Dyson equation, which is, in this specific case, of the form [23]

$$D^{-1}_{ij}(\mathbf{k},\omega) = D^{(0)-1}_{ij}(\mathbf{k},\omega) + \langle V_{ij}\rangle - \sum_{\mathbf{q},m,l} W_{imlj}(\mathbf{q}-\mathbf{k})\,D_{ml}(\mathbf{q},\omega)\,, \tag{12}$$

where $\langle V_{jj}\rangle$ describes the average deformation. This real term is responsible for the phonon frequency shift; it also exists for a homogeneous stress [see Eqn (7)] and would therefore naturally be termed a *homogeneous shift*. The last term in expression (12) is the phonon self-energy given by the Fourier component of the deformation correlator:

$$W_{imlj}(\mathbf{r}-\mathbf{r}') = \left\langle V_{im}(\mathbf{r})V_{lj}(\mathbf{r}')\right\rangle = c\sum_{\mathbf{q}} v_{im}(\mathbf{q})\,v^*_{lj}(\mathbf{q})\exp\left[\mathrm{i}\mathbf{q}(\mathbf{r}-\mathbf{r}')\right]. \tag{13}$$

The imaginary part of the phonon self-energy determines the phonon damping caused by their scattering from defects. The real part will be termed the *inhomogeneous shift*; it results from stress fluctuations.

We recast Eqn (12) in the diagonal form and seek the solution in the form

$$D^{-1}_{jj}(\mathbf{k},\omega) = \Omega_j^2(\mathbf{k},\omega) - s_j^2k^2 - \mathrm{i}\omega\Gamma_j(\mathbf{k},\omega) - \omega^2\,. \tag{14}$$

For the unknown functions $\Omega_j(\mathbf{k},\omega)$ and $\Gamma_j(\mathbf{k},\omega)$ we obtain the system of equations

$$\Omega_j^2(\mathbf{k},\omega) - \omega_0^2 - \langle V_{jj}\rangle - \mathrm{i}\omega\left(\Gamma_j(\mathbf{k},\omega)-\Gamma^{\mathrm{nat}}\right) = \Sigma_{jj}(\mathbf{k},\omega)\,, \tag{15}$$

where the phonon self-energy is

$$\Sigma_{jj}(\mathbf{k},\omega) = -\sum_{m,\mathbf{q}} \frac{W_{jmmj}(\mathbf{q}-\mathbf{k})}{\Omega_m^2(\mathbf{q},\omega) - s^2q^2 - \mathrm{i}\omega\Gamma_m(\mathbf{q},\omega) - \omega^2}\,. \tag{16}$$

We note that in the absence of defects $V_{ij}=0$, $\Sigma_{jj}(\mathbf{k},\omega)=0$, and Eqn (15) gives $\Omega_j(\mathbf{k},\omega)=\omega_0$ and $\Gamma_j(\mathbf{k},\omega)=\Gamma^{\mathrm{nat}}$. In the Born approximation, the correction is obtained with the aid of Eqns (15) by substituting the zero-approximation values in the expression for phonon self-energy (16). If we assume $\Gamma^{\mathrm{nat}}\to 0$ in this case, the already known result (8) is obtained for damping. However, our concern is the value of $\omega=\omega_0$, and the Born approximation is insufficient here.

As already noted, in the investigation of Raman spectra our concern is with small wave vectors $k \ll q_\Gamma, r_v^{-1}$, and therefore the phonon self-energy should be calculated by putting $k=0$. Therefore, the phonon frequency shift and broadening prove to be functions only of ω and are independent of $\mathbf{k}$. To further simplify the calculation of integral (16), the correlation radius r_v may be treated as a cutoff parameter, assuming the correlation function to be a constant $v(q=0)$ for $q<1/r_v$ and equal to zero for $q>1/r_v$.

In the case of point defects, for the contribution of one branch in expression (16) we obtain

$$\Sigma(\omega) = A\left[2b - (a_1-\mathrm{i}a_2)\left(\frac{1}{2}\ln\frac{(b+a_1)^2+a_2^2}{(b-a_1)^2+a_2^2} + \mathrm{i}\arctan\frac{b+a_1}{a_2} + \mathrm{i}\arctan\frac{b-a_1}{a_2}\right)\right], \tag{17}$$

where we introduced the notation

$$a_1 = \left[\Omega^2(\omega)-\omega^2+n^2(\omega)\right]^{1/2},$$

$$a_2 = \left[-\Omega^2(\omega)+\omega^2+n^2(\omega)\right]^{1/2}\operatorname{sign}(\omega)\,,$$

$$n^4(\omega) = \left[\Omega^2(\omega)-\omega^2\right]^2+\omega^2\Gamma^2(\omega)\,, \qquad b=\frac{\sqrt{2}\,s}{r_v}\,.$$

The constant A may be related to either the volume density of defects c_v ($A=c_v v^2(q=0)/4\sqrt{2}\,\pi^2 s^3$) or the deformation fluctuation ε^2 ($A=\varepsilon^2\omega_0^4 r_v^3/2s^3$).

For linear defects,

$$\Sigma(\omega) = B\omega_0\left\{\frac{1}{2}\ln\frac{\left[s^2/r_v^2+\omega^2-\Omega^2(\omega)\right]^2+\omega^2\Gamma^2(\omega)}{\left[\omega^2-\Omega^2(\omega)\right]^2+\omega^2\Gamma^2(\omega)} - \mathrm{i}\arctan\frac{\Omega^2(\omega)-\omega^2}{\omega\Gamma(\omega)} - \mathrm{i}\arctan\frac{s^2/r_v^2-\Omega^2(\omega)+\omega^2}{\omega\Gamma(\omega)}\right\}, \tag{18}$$

where the constant $B=c_\mathrm{s}v^2(q_\perp=0)/4\pi s^2\omega_0$ is proportional to the linear defect density c_s per unit area and can be expressed in terms of the deformation fluctuation $B=\varepsilon^2\omega_0^3 r_v^2/2s^2$.

For planar defects,

$$\Sigma(\omega) = C(-a_1+\mathrm{i}a_2)^{-1}\left[\frac{1}{2}\ln\frac{(b+a_1)^2+a_2^2}{(b-a_1)^2+a_2^2} + \mathrm{i}\arctan\frac{b+a_1}{a_2} + \mathrm{i}\arctan\frac{b-a_1}{a_2}\right], \tag{19}$$

where $C = c_1 v^2(q_z = 0)/\sqrt{2}\,\pi s$ and c_1 is the linear density of planar defects.

The system of integral equations (15) for the functions $\Omega(\omega)$ and $\Gamma(\omega)$ with the phonon self-energy (17), (18), or (19) is easy to solve numerically [23]. In this case, the parameters determining the lineshape are A, B, or C, as well as the parameter b/ω_0, which depends on the correlation radius. When the phonon representation under consideration is degenerate, the coefficients A, B, and C are matrices.

All the aforesaid regarding the effect of short-range defects on the spectral shape of RS applies to the more general Eqn (15) as well. An analysis of this equation for $r_v q_\Gamma > 1$, i.e., for defects with a relatively long radius, suggests that the spectral line is symmetric but its shape is different from the Lorentzian one.

3.1 Stress investigation in the 3*C*-SiC/Si epitaxial heterostructure

Silicon carbide is one of the most popular semiconductor materials, since electronic devices based on silicon carbide can function at high temperatures [24]. Among the numerous hexagonal and rhombohedral polytypes of silicon carbide there is cubic 3*C*-SiC (*C* means cubic and the digit 3 denotes the number of atomic layers which make up the crystal period in the direction of the principal axis).

The theory outlined above was employed to analyze the results of micro-Raman spectroscopic investigations of stress in a film of cubic silicon carbide near the interface with the silicon wafer [25, 26]. The sample geometry is shown schematically in Fig. 5. The 3*C*-SiC film was deposited by vapor-phase heteroepitaxy on a silicon wafer oriented along the normal $\langle 001 \rangle$. Three samples were investigated. The first one was obtained from CRHEA (Valbonne, France). The carbonization temperature was 1400 °C, and the *in situ* monitoring technique was used to stabilize the growth parameters. An 18-μm thick monocrystalline film resulted. The second sample with a thickness of 6 μm was obtained from the LETI-CEA (Grenoble, France); it was distinguished for its low carbonization temperature (1200 °C) and also for the post growth sacrificial oxidation to improve its optical properties. Lastly, use was made of a 3-μm thick sample commercially available from Cree Research, Inc. [27].

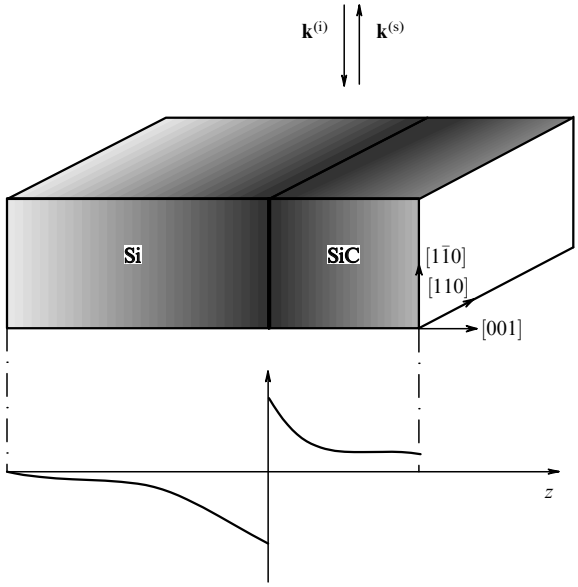

Figure 5. Backscattering geometry in micro-Raman experiments [25]. The laser focal spot was moved along the direction of the $\langle 001 \rangle$ normal towards the SiC/Si interface. The distribution of deformation (compression in the SiC region and tension for Si) is shown in the lower part of the drawing.

The Raman spectra were recorded at room temperature with a Jobin-Yvon T64000 spectrometer equipped with a cooled charge-coupled device (CCD) camera. Use was made of the 5145-Å line of an argon-krypton laser with a power low enough (500 μW) to eliminate sample heating. The light was incident on the clean surface of samples with the $\{1\bar{1}0\}$ orientation (see Fig. 5). A confocal microscope focused the incident beam into a spot about 1 μm in diameter, which was transferred over the $\{1\bar{1}0\}$ sample surface along the $\langle 001 \rangle$ direction. An analysis was made of the Raman spectra in relation to the distance between the light spot and the SiC/Si interface.

The Raman spectra in the neighborhood of the LO mode are shown in Figs 6a, 6c, and 6d. The lineshape is obviously asymmetric for the samples from CRHEA and Cree Research, the low-frequency line wing extending further. This is an indication that the defect correlation radius is rather short. Since the LO mode is a singlet, the spectrum is described by a single coupling constant.

Defect models of varying dimensions were put to a test. The model of linear defects (18) proved to be best suited in our case. The calculated curves are shown by solid lines in Fig. 3, and the results of comparison with theory are given in the caption to Fig. 6 and in Tables 1 and 2 for the CRHEA sample. Also given in Fig. 6b are the functions $\Omega(\omega)$ and $\Gamma(\omega)$ for several distances between the laser spot and the SiC/Si interface, which describe the effect of stress fluctuations on the shift of the resonance curve and its width, respectively. The former function changes sign near the peak of the spectrum; this is the reason why the shift of the resonance frequency is far less than the variation of width. Therefore, the main contribution to the shift is made by the average stress, while its fluctuations define the linewidths.

Table 1. Frequency, width, and inhomogeneous shift of the longitudinal mode in the 3*C*-SiC/Si sample from CRHEA versus distance to the interface; the experimental spectra are shown in Fig. 6c. The last column gives the interaction constant determined from comparison with theory.

Distance, μm	Frequency, cm^{-1}	Width, cm^{-1}	Shift, cm^{-1}	Interaction, cm^{-1}
0	971.6	4.02	0.3	1.5
0.5	972.4	3.86	0.4	1.3
1.0	972.3	3.62	0.3	1.0
2.0	972.5	3.45	0.2	0.7
5.0	973.0	2.88	0.1	0.18
9.0	973.2	2.80	0.1	0.1

Table 2. Frequency and width of the transverse modes in the 3*C*-SiC/Si sample from CRHEA versus distance to the interface; the experimental spectra are shown in Fig. 6e. The last column gives the interaction constant determined in comparison with theory.

Distance, μm	TO_1 frequency, cm^{-1}	TO_1 width, cm^{-1}	TO_2 frequency, cm^{-1}	TO_2 width, cm^{-1}	Interaction B_{zz}, B_{xx}, B_{xz}, cm^{-1}
0	794.0	3.57	796.5	3.12	1.8, 1.4, 0.3
0.5	795.3	3.33	797.0	3.07	1.4, 1.3, 0.3
1.0	795.4	2.43	796.8	2.34	0.5, 0.5, 0.1
2.0	796.1	2.09	797.1	2.04	0.2, 0.2, 0.05
5.0	797.0	2.03	797.8	1.97	0.2, 0.15, 0.01
9.0	797.0	2.01	797.6	1.95	0.1, 0.1, 0.07

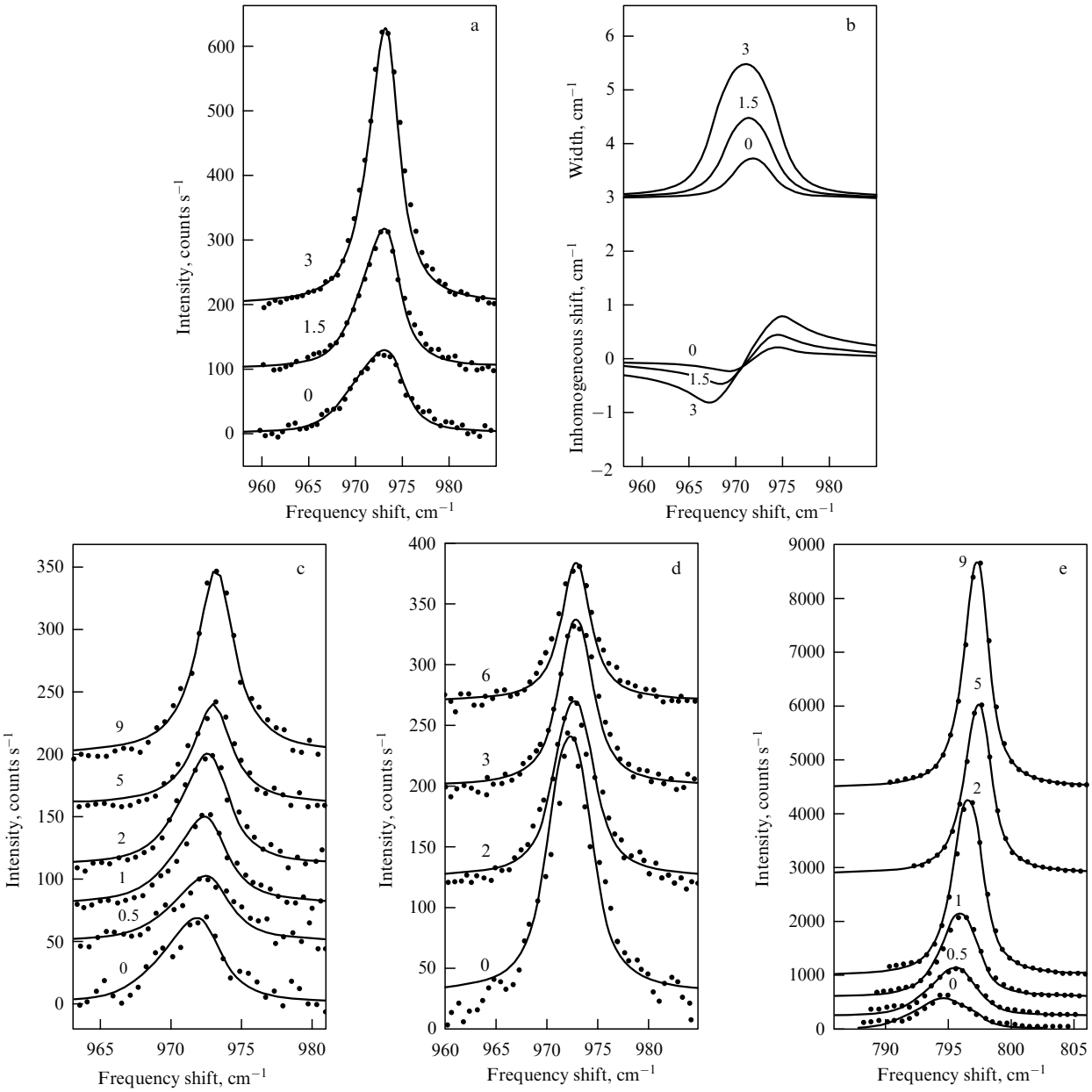

Figure 6. Spectra of RS from the side surface of monocrystalline SiC films of varying thickness deposited on a silicon wafer: (a, c, d) for the longitudinal mode of samples with respective film thicknesses of 3, 18, and 6 μm; (e) for the transverse mode of an 18-μm film. The distance between the laser spot and the SiC/Si interface is specified by the curves in micrometers. The curves were plotted by way of comparison with theory, Eqns (15) and (18). (b) Functions $\Gamma(\omega)$ (top) and $\Omega(\omega)$ (bottom) corresponding to the spectra of Fig. 6a. The line position and width, as well as the interaction constant B, derived by this comparison for different distances between the light spot and the SiC/Si interface are collected in Tables 1 and 2 for an 18-μm film sample. The corresponding values (cm^{-1}) for the curves in Fig. 6a: (0 μm) 972.7, 5.2, 3.0; (1.5 μm) 972.9, 4.3, 1.5; (3 μm) 973.1, 3.6, 0.7; and in Fig. 6d: (0 μm) 972.4, 4.38, 20; (2 μm) 972.8, 4.11, 15; (3 μm) 973.0, 3.66, 8; (6 μm) 973.0, 3.29, 3.2.

The correlation radius for all curves in Figs 6a and 6c was found to be the same, $r_v\omega_0/s = 20$, which corresponds to $r_v/a \simeq 6$. The LO mode lineshape for the LETI-CEA sample shown in Fig. 6d is symmetric but not Lorentzian. This situation corresponds to a relatively long-range correlation function, $r_v/a = 25$. The natural width of the longitudinal phonon ranges between 2.8 and 3.0 cm^{-1} for different samples, the small difference being related to the quality of the samples.

The effect of stress fluctuations is also evident in the TO-phonon range. The experimental results obtained with the CRHEA sample are given in Fig. 6e. The TO phonon is a doublet, and its stress-induced splitting is seen in the spectrum recorded for the shortest distance from the interface. The line asymmetry is visible in the spectra with distances to the interface of 1, 2, 5, and 9 μm, where the spacing of the doublet is rather small: the low-frequency line wing falls off more slowly than the high-frequency one. We note that the natural linewidth proved to be the same for all lines of transverse modes: $\Gamma^{\text{nat}} = 1.8$ cm^{-1}. The correlation radius also proved to be the same: $r_v/a \simeq 6$.

Using the expression for the coupling constant $B_{jm} = \varepsilon^2\omega_0^3 r_v^2/2s^2$ it is possible to estimate the deformation fluctuation versus distance between the spot and the SiC/Si interface [compare Eqns (18) and (12)]. This dependence is depicted in Fig. 7, which indicates that the deformation relaxes primarily

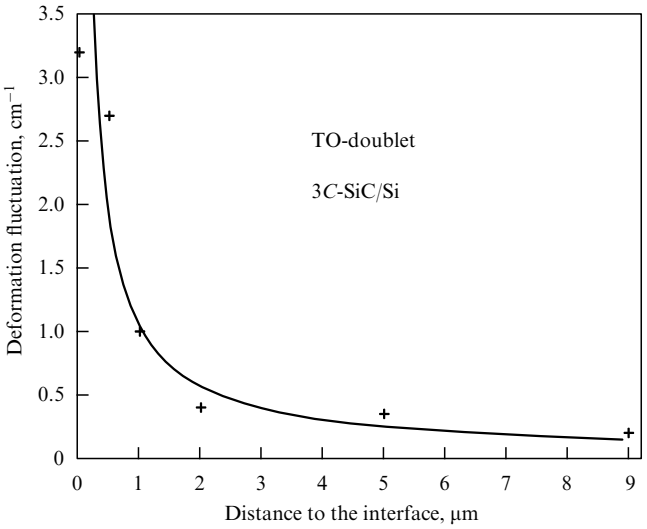

Figure 7. Variation of the fluctuation part of deformation at a distance z to the interface: points show the value $B_{xx} + B_{zz}$ from Table 2, the curve shows the dependence $1/z$.

at a distance on the order of 3 μm. This relaxation can be approximated by the $z^{-\alpha}$ law. The rms fitting yielded $\alpha = 1.0 \pm 0.2$. Similar fitting for the LO phonon resulted in $\alpha = 0.76 \pm 0.25$, i.e., in the same value to within experimental error. Employing the values $r_v/a = 6$ and $B = 2$ cm^{-1}, the deformation was estimated as $\varepsilon \simeq 10^{-3}$ at a distance of about 0.25 μm from the interface.

3.2 Investigation of the Raman spectra at silicon – insulator interfaces

References [28, 29] were concerned with the study of deformation fluctuations near the silicon – insulator interfaces. These silicon-on-insulator (SOI) structures have recently found wide use (see, for instance, Refs [30, 31]), since they make it possible to avoid direct electric contact between the active part of the device and the wafer. A conventional SOI structure is depicted in Fig. 8. A thin monocrystalline silicon overlayer (SOL) is on top of the buried silicon oxide (BOX) layer, which in its turn resides on a thick silicon wafer. The monocrystalline film is normally 0.2 μm thick and the oxide layer is 0.4 μm. To produce the oxide, two different methods are in fact used: one involving oxygen ion implantation termed SIMOX (separation by implantation of oxygen) and the other involving hydrophilic bonding of two pre-oxidized silicon layers, called the BESOI method (bond and etch back SOI) or Unibond [32].

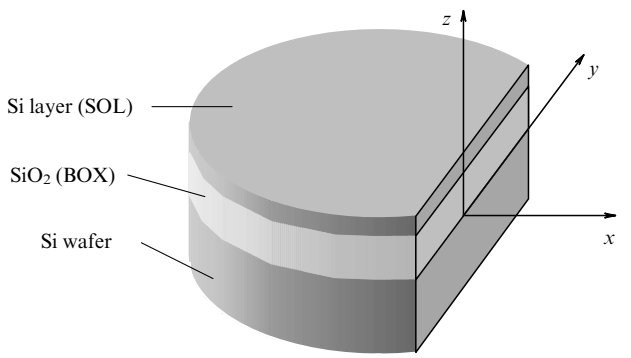

Figure 8. Schematic of an SOI sample in the RS experiment. The laser beam was incident on the face plane in the x direction and was shifted along the normal to the silicon wafer (the z-axis) to investigate the stress in it; there was no way of doing this in the SOL and BOX layers owing to their small thickness.

The experiments were conducted on three samples 100 mm in diameter prepared in SOITEC [32]; one was prepared by the SIMOX method by way of intense oxygen implantation and the other two by the Unibond method. In all cases, the initial Si film thickness was 0.2 μm. In two cases (the Unibond and Simox samples), advantage was taken of sacrificial oxidation to reduce the film thickness (the experimental series A and B). To estimate the effect of multiple high-temperature oxidation at 1050 °C, one more Unibond sample was subject to a low-temperature oxygen-assisted IBE (ion beam etching) process (the C experimental series).

Of course, the goal is that all three layers (SOL, BOX, and the silicon wafer) should be void of defects and stress. However, the real situation is not nearly so ideal. According to the data available from the literature, the SOL surface roughness ranges from 2 Å in the Unibond sample to 5 Å in the SIMOX one, while the dislocation density ranges from 10^2 cm^{-2} in the Unibond sample to 10^6 cm^{-2} in the SIMOX one. Direct bonding of two oxidized films should result, like the ion implantation accompanied by high-temperature annealing, in the emergence of stress at the interface [33]. This gives rise to defects in the SOL as well, primarily to dislocations. The interaction between dislocations and stress in a solid is a well-known problem of the theory of elasticity. Recent years have shown certain progress in this direction [34 – 36], but many qualitative observations remain to be explained.

3.2.1 Investigation of the Raman spectra from samples with varying Si film thickness. Since the SOL is too thin for the investigation of its properties even by micro-Raman spectroscopy, the reflected signal in Ref. [29] was recorded from the side plane of the wafer. In this case, the spectrum variation in the backscattering geometry was recorded in relation to the SOL thickness, which varied from approximately 200 to 5 nm. For each layer of specific thickness, several spectra were recorded in the x direction, the spectra corresponding to different distances between the laser beam and the wafer – BOX interface (see Fig. 8). Some results of investigation of the Raman spectra from the A series samples are shown in Fig. 9.

The experimental data were compared with the calculated data starting from Eqns (11) – (14) of the theory. Owing to the presence of the interface, the triplet of optical phonons for $k = 0$ splits into a doublet corresponding to vibrations in the interface plane (the x and y directions) and a singlet corresponding to vibrations in the z direction. In the matrix of coupling constants, the nonzero elements are $B_{xx} = B_{yy}$, $B_{xz} = B_{yz}$, and B_{zz}. The numerical solution of Eqns (15) and (18) yields the coefficients B_{ij}, which define the shift and width of the line. The linear defect model provides the best description of experimental data in this case. Figure 6d gives one example of a numerical solution [the functions $\Gamma_j(\omega)$ and $\Omega_j(\omega) - \omega_0 - \langle V_{jj}\rangle/2]$ for $j = z$, i.e., for a z-polarized phonon. The results of comparison with theory — the positions of resonances, their widths, and the values of the matrix elements B_{xx} and B_{zz} — are collected in Table 3 for the A series samples (Unibond); the B_{xz} coefficient did not prove to have any effect and was therefore set equal to zero. The best agreement was reached for $r_v\omega_0/s = 16$, which corresponds to a correlation radius (the dislocation core size) $r_v = 1.3$ Å.

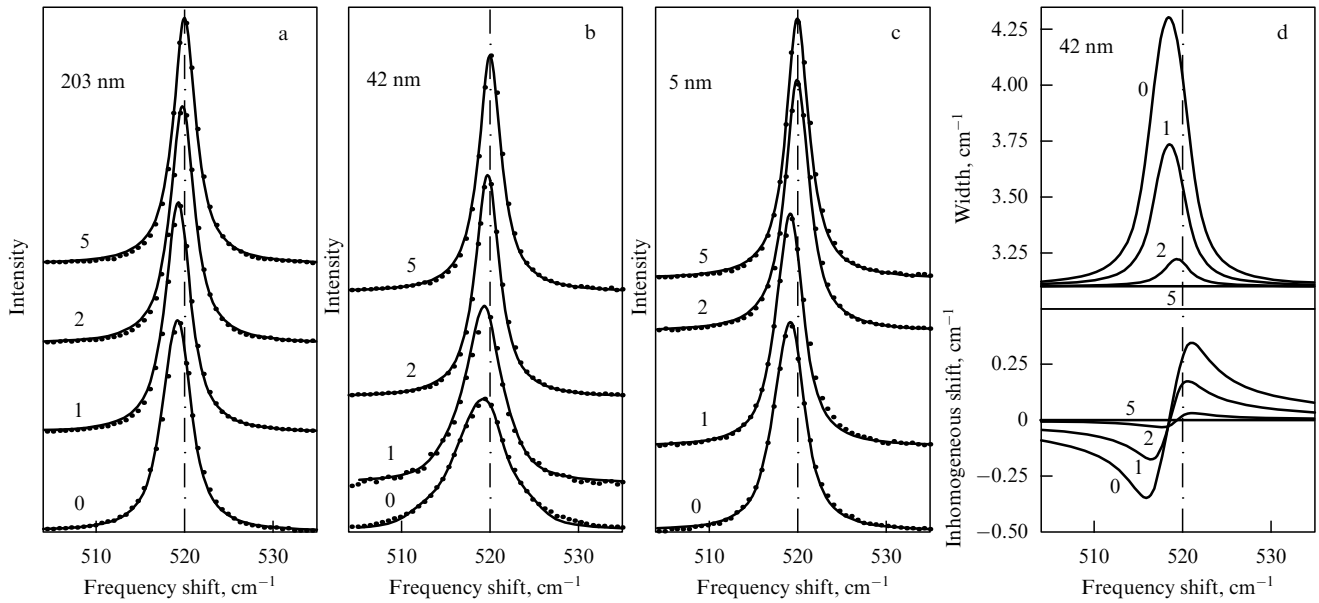

Figure 9. Raman spectra (points are experiment, curves are theory) from silicon crystals (A sample series) with SOLs of different thickness (203, 42, and 5 nm) and at varying distances (indicated by the curves) between the laser beam and the BOX layer. The dash-dot lines indicate the location of the spectrum maximum for the greatest distance. The theoretical dependences $\Gamma(\omega)$ (top) and $\Omega(\omega)$ (bottom) derived by solving Eqns (15) and (18) are given for the 42-nm thick sample (d).

Table 3. Frequency, width, and interaction with defects for phonons Γ'_{25} in Unibond samples with different SOL thickness for different distances to the interface.

Layer thickness, nm	Distance to the interface, μm	Γ'_{25} frequency, cm^{-1} ω_z, ω_x	Width, cm^{-1} Γ_z; Γ_x	Interaction, cm^{-1} B_{zz}, B_{xx}
203	5.0	520.0	3.10	0
	2.0	519.76	3.21	0.20
	1.0	519.28	3.32	0.39
	0	519.18	3.61	0.97
95	5.0	520.0	3.10	0
	2.0	520.0	3.10	0
	1.0	520.0	3.32	0.38
	0	519.28	3.69	1.16
42	5.0	520.0	3.10	0
	2.0	520.0	3.21	0.19
	1.0	519.18, 516.13	3.69, 3.26	1.16, 0.29
	0	519.17, 519.08	4.25, 3.42	2.51, 0.6
11	5.0	520.0	3.10	0
	2.0	520.18, 520.15	3.32, 3.1	0.38, 0
	1.0	520.27, 520.22	3.86, 3.42	1.54, 0.58
	0	519.55, 519.13	6.23, 3.70	9.6, 1.2
5	5.0	520.0	3.10	0
	2.0	519.73, 519.70	3.32, 3.1	0.39, 0
	1.0	519.26, 519.27	6.44, 3.61	10.6, 0.96
	0	519.14, 519.00	9.44, 4.65	29.0, 3.67

We note that both the width and the resonance frequency (520 cm^{-1}) of the Raman spectrum assume its bulk values for the longest distance between the laser spot and the interface (about 5 μm for all samples of the series). As the spot–interface distance shortens (2 μm first, then 1 μm), the line shifts towards lower frequencies and broadens, which is particularly significant for a small SOL thickness. This becomes noticeable for a film thickness below 42 nm.

The theory enables us to distinguish two contributions of defects to the phonon frequency shift. The first-order contribution is independent of the phonon frequency but is responsible for the common shift and splitting of the optical phonon triplet in silicon. The shift to the low-frequency side is indicative of the presence of tensile stress in the surface wafer layer [8, 25]. The splitting of the triplet to a singlet and a doublet, which is allowed by the symmetry, is noticeable only for sufficiently thin SOLs (5 and 11 nm, see Table 3). One more contribution to the line shift arises in the second order of the perturbation theory; it depends on the frequency (Fig. 9d) and defines the linewidths. One can see from Table 3 that the magnitude of the second contribution, for instance for an SOL thickness of 5 nm, amounts to 6.1 cm^{-1} for the linewidths and +0.36 cm^{-1} for the line frequencies. We note that this contribution to the shift is appreciably smaller than the first-order contribution, which amounts to −1.2 cm^{-1} for the same sample.

Similar results were also obtained for the SIMOX. The natural width was found to be somewhat larger (3.4 cm^{-1} in comparison with 3.1 cm^{-1} for Unibond) and the correlation radius corresponded to the same value $r_v\omega_0/s = 16$. The main distinction is that the stress relaxation depth is larger in this case. Specifically, some difference in linewidth can be seen at distances of 5 and 20 nm from the interface.

Therefore, an unexpected effect was discovered: for a fixed laser spot–interface distance, the width of Raman lines in the wafer increased with a reduction in the SOL thickness. As this distance increases, the lines become narrower to attain a value defined by the natural width at a distance of several micrometers. This is an indication that the stress in the wafer increases as the SOL thickness is reduced. This stress relaxes at a distance of several micrometers from the Si/SiO_2 interface. To verify this conclusion, investigations were made of the infrared reflection by the SOL surface and its roughness.

3.2.2 Effect of SOL thickness on the infrared reflection. A study was made of the interference in the infrared reflection in the 400–7500 cm^{-1} frequency range to control the SOL thickness [37]. Along with the interference pattern, a

singularity was observed in the 1000 – 1100 cm^{-1} range. This singularity was clearly seen to become narrower with reduction of the SOL thickness from 203 to 95 and then to 42 nm. The origin of the 1070 – 1080 cm^{-1} doublet structure is well known [38 – 43]: it is caused by the splitting of the triply degenerate vibration of the SiO_4 tetrahedron residing in the BOX. The presence of the interface changes the symmetry of the field surrounding the tetrahedron and the z mode splits off the x and y vibrations, so that a doublet structure with a 1 : 2 intensity ratio is observed. The relatively broad singularity in the initial sample with an SOL thickness of 200 nm splits into two separate vibrations when the SOL thickness becomes less than 40 nm. Based on the intensity ratio, the lower frequency value is ascribed to the z vibration, while their common shift to the lower frequency side testifies to the compressive character of the stress in the oxide layer. To account for the singularity narrowing, the stress in the SOL may be assumed to decrease as the thickness is reduced. The relative variation of the bond length in the molecule can be estimated by approximating the potential energy by the power law r^{-n}, where n is close to five for typical oxides. Then, the relative variation in the vibration frequency is $\delta\omega/\omega = (n+2)\,\delta r/2r$. Since the reduction of SOL thickness results in a frequency shift of 50 cm^{-1}, the variation of the Si – O bond length is estimated as 1%.

3.2.3 Correlation of Raman spectra with surface roughness. Measurements of surface roughness with a tunnel microscope [29] showed that the rms roughness increased from 1.5 to 4 Å as the SOL thickness was lowered from 203 to 5 nm. Clearly there is a direct relationship between the surface roughness and the elastic stress near the interface. By averaging roughness over a sufficiently large surface area it is possible to obtain the equation

$$\zeta^2 - \zeta_0^2 = c b_0^2 l^2 ,$$

which relates the average roughness ζ^2 to the dislocation density c in the surface layer of the SOL. Here, ζ_0^2 is the roughness in the absence of dislocations, b_0 is, by the order of magnitude, the Burgers vector, and l is the average size of hills on the surface in the tangential direction generated by the roughness. On the other hand, with the use of Eqn (18), for the maximal width [at the line center $\omega = \Omega(\omega)$] we have

$$\Gamma - \Gamma^{\mathrm{nat}} = \alpha(\zeta^2 - \zeta_0^2) \arctan \frac{s^2}{r_v^2 \omega_0 \Gamma} , \qquad (20)$$

where $\alpha = r_v^4 \omega_0^3 / 4\pi s^2 b_0^2 l^2$.

The dependence (20) is shown with a solid line in Fig. 10, together with experimental points for samples with various SOL thicknesses. The only fit parameter $\alpha = 2.1$ cm^{-1} $Å^{-2}$ was selected so that the lines pass through the values of z-phonon width and roughness measured for the sample with a 5-nm thick SOL. The value $\alpha = 0.28$ cm^{-1} $Å^{-2}$ for the x phonon was obtained by comparing the constants B_{xx} and B_{zz} from Table 3. It is instructive to estimate the surface roughness parameter l employing these data. We take the expression for α and put $b_0 = 1$ Å to obtain a reasonable value for the dimension of hills on the surface: $l = 88$ Å. The samples obtained in different ways differ by the values of initial roughness (1.2 Å, the A series) and (2.0 Å, the C series).

The main conclusion of the work is that the SOL samples make up a balanced system depicted schematically in Fig. 11.

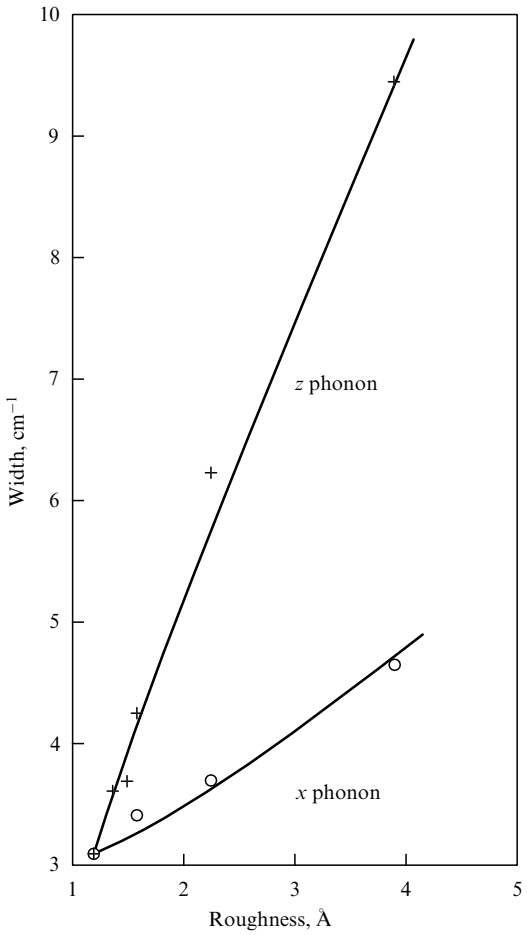

Figure 10. Widths of the two components of the phonon triplet as functions of the mean square roughness of the SOL surface of the A-series samples. The points represent the experimental data for layers of different thicknesses (203, 95, 42, 11, and 5 nm), the curves were plotted using Eqn (20).

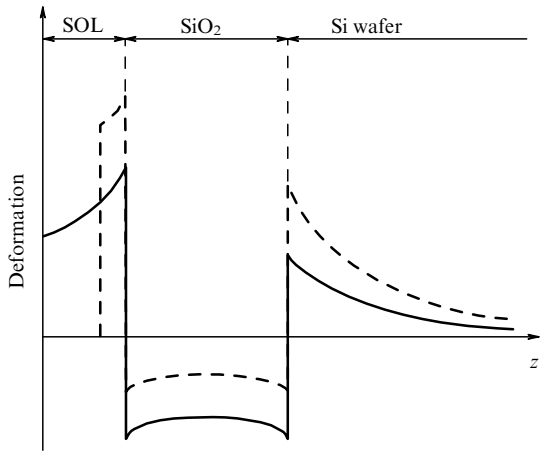

Figure 11. Stress distribution in an SOI sample for two thicknesses of the surface SOL.

The distinctive features of this system are, first, the presence of compression stress in the oxide layer, which lowers with a reduction in the SOL thickness and, second, the tensile stress in the SOL, on whose surface there occurs a roughness of up to 4 Å if the layer is thin enough. And, lastly, there is a tensile and fluctuating stress in the wafer leading to a deformation on

the order of 10^{-2}. The source of this stress is the Si/SiO_2 interface between the materials with different coefficients of thermal expansion, as well as with different lattice constants. The oxide layer borders on silicon regions on either side, and therefore thinning one of them (the SOL) results in an increase in the tensile stress of the other (the wafer). At the same time, the compression stress in the oxide layer decreases.

3.3 Resonance interaction of propagating and localized phonon modes

Up to this point we considered the interaction of propagating phonon modes with defects. At the same time, local phonon vibrations can also arise in the presence of defects [44–46]. There exists an important distinction between point defects on the one hand and linear or planar defects on the other. In the latter case, according to quantum mechanics, localized states may occur at the continuum edge ω_0 due to a relatively weak phonon–defect interaction. We then encounter the serious problem of taking into account the resonance interaction of localized modes and propagating modes of the continuum.

Numerical calculations invoking different models [47, 48] were conducted in order to determine the effect of planar stacking faults on the phonon spectrum of SiC polytypes. To solve the problem in the analytical form [49], advantage is conveniently taken of the Green function technique. Assuming the defect potential to be short-range [$v(\mathbf{q}) = v_0$ in Eqn (13)] and retaining the terms of higher order in this potential than was previously done, we obtain the Dyson equation for the phonon Green function in the form

$$D(\mathbf{k},\omega)^{-1} = D_0(k,\omega)^{-1} + cv_0\left(1 + v_0\sum_{\mathbf{q}} D(\mathbf{q},\omega)\right)^{-1}, \quad (21)$$

where the last term is the phonon self-energy in the approximation linear in the density c. We restricted ourselves to the case of low defect density, when the average distance between the defects ($r_c \propto c^{-1/2}$ for linear defects) is long in comparison with the phonon mean free path. We note two circumstances: first, if Eqn (21) is expanded in powers of v_0 we arrive at an equation of the Eqn (12) type. Second, when D_0 is substituted for D in the integral and the imaginary part is separated, in the limit $\Gamma \to 0$ there emerges expression (8) obtained in the second order in v_0.

The poles of the Green function yield the spectrum of the system. In the absence of defects, these are the propagating phonon states, to which there correspond the poles of D_0. When there is only one defect, D_0 should be substituted instead of D in the expression for phonon self-energy, and then, for the proper sign of the coupling constant, a pole can emerge, which describes the localized state. The frequency of this state is derived from the equation

$$1 + v_0\sum_{\mathbf{q}} D_0(\mathbf{q},\omega) = 0\,.$$

However, for a finite density of defects, D should be kept inside the integral sign. The resultant equation (21) is an integral equation for the Green function $D(\mathbf{q},\omega)$. This equation takes into account the resonance interaction of the localized states and the continuum states.

The integral equation can be reduced to an algebraic one [49]. To this end, in the case of point defects we introduce a new unknown function ζ and a complex variable ζ_0:

$$D(\mathbf{k},\omega) = (\zeta - s^2k^2)^{-1}, \qquad \zeta_0 = \omega_0^2 - \omega^2 - i\omega\Gamma^{\text{nat}}\,.$$

Then, Eqn (21) gives

$$\zeta = \zeta_0 + c\omega_0^3\left(\frac{\kappa}{\lambda} - \kappa + \frac{\pi}{2}\sqrt{-\zeta}\right)^{-1}. \quad (22)$$

For linear defects,

$$D(\mathbf{k},\omega) = (\zeta - s^2k_\perp^2)^{-1}, \qquad \zeta_0 = \omega_0^2 - s^2k_z^2 - \omega^2 - i\omega\Gamma^{\text{nat}},$$

and we obtain

$$\zeta = \zeta_0 + c\omega_0^2\left(\frac{1}{\lambda} - \ln\frac{\kappa^2}{-\zeta}\right)^{-1}. \quad (23)$$

For planar defects,

$$D(\mathbf{k},\omega) = (\zeta - s^2k_z^2)^{-1}, \qquad \zeta_0 = \omega_0^2 - s^2k_\parallel^2 - \omega^2 - i\omega\Gamma^{\text{nat}},$$

and we find

$$\zeta = \zeta_0 + c\omega_0^2\left(\frac{1}{\lambda} - \frac{\omega_0}{\sqrt{-\zeta}}\right)^{-1}, \quad (24)$$

where λ is the dimensionless phonon–defect coupling constant proportional to v_0; c is the dimensionless atomic density of defects per unit volume, area, or length for point, linear, or planar defects, respectively; $\kappa \sim s/a$ is the cutoff parameter, which is on the order of the Debye frequency; the z-axis is aligned with the direction of the linear defect; and the two-dimensional vector $\mathbf{k}_\parallel$ is selected along the planar defect. The values of the functions $\sqrt{-\zeta}$ and $\ln(-\zeta)$ are taken in the upper complex half-plane.

Each of Eqns (22)–(24) is in fact a system of two equations for the real and imaginary parts of ζ. In this case, instead of ζ we can conveniently introduce real variables x and y:

$$-\zeta = \sqrt{x^2+y^2}\exp\left[i\left(\frac{\pi}{2} - \arctan\frac{x}{y}\right)\right],$$

assuming that $y > 0$ and $-\pi/2 < \arctan z < \pi/2$ in accordance with the choice of the function values defined above. A similar form is also employed for ζ_0 with the change $x \to \omega^2 - \omega_0^2$ and $y \to \omega\Gamma^{\text{nat}}$. We calculate $\operatorname{Im}\zeta^{-1}$ to find the Raman spectrum with the excitation of a long-wave ($k = 0$) optical phonon.

Two calculated Raman spectra for planar defects are exemplified in Fig. 12. The calculations were made under the assumption that the optical phonon branch has a maximum at the center of the Brillouin zone at a frequency $\omega_0 = 520\ \text{cm}^{-1}$ for $k = 0$. One can see from Fig. 12a (the coupling constant is negative and the localized state is absent) that the resonance line corresponding to the excitation of the long-wavelength phonon is asymmetric. The broadening is stronger on the low-frequency side of the peak, which results in asymmetry. This is the effect of the final-state phonon density: the elastic interaction with defects contributes to the phonon width only in the $\omega < \omega_0$ range, to which phonon transitions can occur in the scattering by defects.

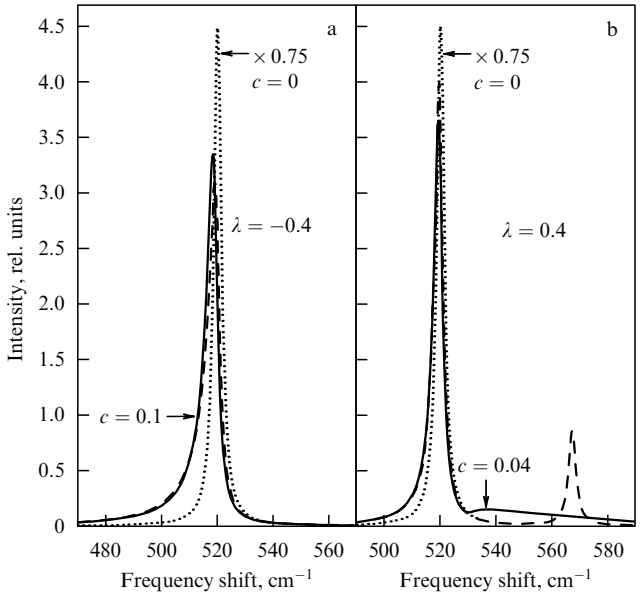

Figure 12. Raman spectra (solid curves) obtained by solving Eqn (24) in the presence of planar defects for negative (a) and positive (b) values of the coupling constant λ; c is the defect density per unit length. The Born approximation is shown with dashed lines. In this approximation, the local vibration is represented with a peak at $\omega = 570$ cm^{-1} (b), which disperses in the exact solution. For $c = 0$, the spectra are shown with dotted lines.

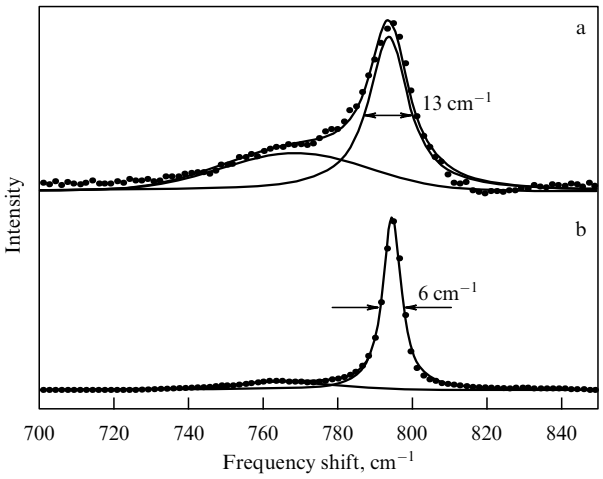

Figure 13. Raman spectra of 3*C*-SiC with planar defects, from Ref. [40]: (a) prior to annealing, (b) after annealing.

When the coupling constant is positive (Fig. 12b), there exist localized states with frequencies above the continuum edge $\omega > \omega_0$. Their contribution to the Raman spectrum has the form of an extensive continuum with a width proportional to $\sqrt{c}$. This dependence results from the resonance interaction of localized states with the nearby continuum. Had we substituted the zero-approximation function D_0 instead of D on the right-hand side of the Dyson equation (21), we would have obtained the conventional form of local vibration spectrum with a maximum (shown with a dotted line). This spectrum does not differ from the exact one only when there is a large coupling constant, so that localized states occur away from the continuum edge. Their contribution to the Raman spectrum is Lorentzian in form and significantly smaller in magnitude, which is proportional to the defect density in this case.

We note that the localized states are related to the minimum of the optical phonon branch for a negative value of the coupling constant, and their frequencies then lie below the continuum edge. Numerical calculations carried out in Ref. [47] yielded the corresponding spectrum pattern (Fig. 13) with a broad plateau.

4. Coulomb effects in a uniaxial semiconductor

It is well known [50] that the Coulomb field excited in the optical vibrations in lattices with a dipole moment (for instance, in SiC) lifts the threefold degeneracy at the center of the Brillouin zone. The frequency of longitudinal optical vibrations comes to exceed the frequency of the transverse ones. In non-cubic crystals (for instance, in hexagonal and rhombohedral polytypes of the same SiC), one more effect is related to the Coulomb field. Namely, optical vibration frequencies prove to be dependent on the direction of phonon propagation: for $k = 0$, the *frequencies depend on the direction of the wave vector* $\mathbf{k}$. This is a relatively unusual effect, both from the physical and mathematical standpoints: the eigenvalues of dynamic matrix calculated for $\mathbf{k} = 0$ are nevertheless dependent on the vector $\mathbf{k}$. The reason for this effect lies with the non-analytic dependence of the dynamic matrix on the direction of $\mathbf{k}$, which is caused by the long-range Coulomb field.

As already noted, in micro-Raman spectroscopy both incident and reflected light beams are focused. In this case, the Raman line in a non-cubic crystal proves to be more strongly broadened because the absorbed phonon frequency depends on the direction of its wave vector.

The effects of long-range dipole – dipole interaction have been known in ferroelectrics [51]. Recent numerical calculations [52, 53] clearly reveal the dependence of optical phonon frequencies on the direction of the wave vector at the center of the Brillouin zone in A^3B^5-type semiconductors.

However, for uniaxial SiC polytypes the problem can be solved without resorting to numerical calculations, by invoking only symmetry considerations [54]. First, we consider the phonon spectrum of the 3*C*-SiC cubic polytype, whose elementary cell contains two atoms. For the close neighborhood of the center of the Brillouin zone, where $k \ll \pi/a$ (a is the lattice constant), it is possible to split the acoustic and optical modes by expanding the dynamic matrix in powers of the vector $\mathbf{k}$. For optical modes in the zero approximation in $\mathbf{k}$ there results a system of three equations of the form

$$(\phi - M'\omega^2)\mathbf{u} = \mathbf{f}, \tag{25}$$

where M' is the reduced mass of the two atoms (Si and C) in an elementary cell and ϕ is the diagonal element of the interaction matrix (in a cubic crystal there exists only one such element of a 3×3 matrix). When calculating ϕ it is always possible to restrict oneself to some number of closest neighbors. However, the effect of the long-range Coulomb field cannot be included in this way. It can be represented as the force $\mathbf{f} = Z\mathbf{E}$ acting on the effective charge Z, and the electric field $\mathbf{E}$ itself should be determined from the given optical displacement field $\mathbf{u}$ with the aid of the Maxwell equations.

Eliminating the magnetic field from the Maxwell equations, it is possible to express the electric field **E** in terms of the polarization **P**:

$$\mathbf{E} = \frac{-4\pi\left[\mathbf{k}(\mathbf{kP}) - \omega^2\mathbf{P}/c^2\right]}{k^2 - \omega^2/c^2}\,. \tag{26}$$

The frequency ω, which is of interest here, is on the order of the optical phonon frequency, i.e., 10^3 cm^{-1}, and the wave vector of the phonon, when it is excited by light, is by the order of magnitude equal to the wave vector of the light (in Raman scattering it is defined by the transferred momentum), which amounts to 10^5 cm^{-1}. This implies that the condition $k \gg \omega/c$ is satisfied (the region where this condition is violated is termed the polariton region). Then, in expression (26) the terms with c^2 should be neglected, with the result that the electric field – polarization relationship assumes a simple and singular form:

$$\mathbf{E} = \frac{-4\pi\mathbf{k}(\mathbf{kP})}{k^2}\,. \tag{27}$$

In the long-wavelength approximation ($k \ll \pi/a$), which we restrict ourselves to, the polarization is related to the dipole moment of an elementary cell $Z\mathbf{u}$: $\mathbf{P} = NZ\mathbf{u} + \chi\mathbf{E}$, where χ is the atom polarizability and N is the number of elementary cells per unit volume. Expressing **E** in terms of **u** with the aid of the last-given expressions and employing the equations of motion (25), for a cubic crystal we find the frequencies of transverse ($\omega_{\mathrm{TO}}^2 = \phi/M$) and longitudinal ($\omega_{\mathrm{LO}}^2 = \phi/M + \omega_{\mathrm{pi}}^2$) optical phonons, where

$$\omega_{\mathrm{pi}} = \left(\frac{4\pi NZ^2}{M'\varepsilon_\infty}\right)^{1/2}$$

is the ion plasma frequency and $\varepsilon_\infty = 1 + 4\pi\chi$. Despite the fact that the direction of the vector **k** appears explicitly in the relationship between **E** and **P**, the optical vibration frequencies are *direction-independent*, as they must be for a cubic crystal.

As is well known, the anisotropy of non-cubic SiC polytypes is small, because the nearest environment retains cubic symmetry. We introduce the static deformation tensor u_{ij}, which will describe the difference between the elements of the dynamic matrix of a non-cubic polytype and a cubic one. Then, the phonon spectrum of the non-cubic polytype can be derived as follows. At first we expand the interaction matrix in powers of u_{ij} and find the frequencies of so-called 'strong' modes. Then, account should be taken of the fact that there are more than two atoms in the elementary cell of a non-cubic polytype, resulting in the emergence of additional 'weak' optical modes. They can be obtained by folding the Brillouin zone of the cubic polytype in the direction of the principal axis the number of times corresponding to the increase in the number of atoms in the elementary cell. The folding procedure was proposed in Ref. [55], while the frequency shifts and the intensities of weak modes in optical absorption and Raman scattering were calculated in Ref. [56].

The dynamic matrix may contain only invariants (with respect to crystal symmetry transformations) composed of components of the u_{ij} tensor. There exist two such first-order invariants u_{zz} and $u_{xx} + u_{yy}$ in crystal axes. Furthermore, it is always possible to fix the volume of the initial imaginary crystal, i.e., put $u_{ii} = 0$. Only one invariant remains, for instance u_{zz}, and it can be written by adding only to the zz element. Finally, account can also be taken of the small anisotropy of the polarizability tensor, whose two principal values χ_{xx} and χ_{zz} are different in a uniaxial crystal. Therefore, for strong modes there results, in lieu of Eqns (25), the system of equations

$$\begin{pmatrix} \beta + \tilde\omega_{\mathrm{pi}}^2 n_x^2 - \omega^2 & \tilde\omega_{\mathrm{pi}}^2 n_x n_y & \tilde\omega_{\mathrm{pi}}^2 n_x n_z \\ \tilde\omega_{\mathrm{pi}}^2 n_x n_y & \beta + \tilde\omega_{\mathrm{pi}}^2 n_y^2 - \omega^2 & \tilde\omega_{\mathrm{pi}}^2 n_y n_z \\ \tilde\omega_{\mathrm{pi}}^2 n_x n_z & \tilde\omega_{\mathrm{pi}}^2 n_y n_z & \alpha + \tilde\omega_{\mathrm{pi}}^2 n_z^2 - \omega^2 \end{pmatrix} \times \begin{pmatrix} u_x \\ u_y \\ u_z \end{pmatrix} = 0\,, \tag{28}$$

where

$$\mathbf{n} = \frac{\mathbf{k}}{k}\,, \qquad \alpha = \frac{\phi}{M'}\,, \qquad \beta = \alpha + bu_{zz}\,,$$

$$\tilde\omega_{\mathrm{pi}}^2 = \frac{4\pi NZ^2}{M'\left[1 + 4\pi(\chi_{xx}\sin^2\theta + \chi_{zz}\cos^2\theta)\right]}\,.$$

We select the yz plane in such a way that the vector **k** lies in this plane and denote by θ the angle between **k** and the z-axis: $n_x = 0, n_z = \cos\theta$, and $n_y = \sin\theta$. Then, the Coulomb part of the matrix (28) is diagonalizable with the unitary transformation

$$U_{ij} = \begin{pmatrix} 1 & 0 & 0 \\ 0 & \cos\theta & \sin\theta \\ 0 & -\sin\theta & \cos\theta \end{pmatrix} \tag{29}$$

and the problem of phonon frequency determination reduces to the diagonalization of the matrix

$$\begin{pmatrix} \beta & 0 & 0 \\ 0 & \beta\cos^2\theta + \alpha\sin^2\theta & (\beta - \alpha)\sin\theta\cos\theta \\ 0 & (\beta - \alpha)\sin\theta\cos\theta & \beta\sin^2\theta + \alpha\cos^2\theta + \tilde\omega_{\mathrm{pi}}^2 \end{pmatrix}. \tag{30}$$

The solution of this problem is evident. There is one transverse vibration (TO_1) with the frequency $\omega_{\mathrm{TO}_1}^2 = \beta$, polarized in the x direction, and two modes in the yz plane with the frequencies

$$\omega_{2,3}^2(\theta) = \frac{1}{2}(\tilde\omega_{\mathrm{pi}}^2 + \alpha + \beta) \pm \frac{1}{2}\left\{\left[\tilde\omega_{\mathrm{pi}}^2 + (\alpha - \beta)\cos 2\theta\right]^2 + (\alpha - \beta)^2\sin^2 2\theta\right\}^{1/2}. \tag{31}$$

We emphasize that expression (31) gives the optical phonon frequencies at the center of the Brillouin zone, but they depend on the wave vector direction. This dependence arises from the combined effect of the Coulomb field and crystal anisotropy. In the absence of the Coulomb field ($\tilde\omega_{\mathrm{pi}}^2 = 0$), the frequencies are $\omega_2^2 = \alpha$, $\omega_3^2 = \beta$, and there is no angular dependence. In the isotropic case ($\alpha = \beta$, $\chi_{xx} = \chi_{zz}$), formula (31) gives the spectrum of a cubic crystal.

In the limiting case when the crystal anisotropy is small in comparison with the Coulomb interaction ($|\alpha - \beta| \ll \omega_{\mathrm{pi}}^2$), one of the yz modes proves to be almost transverse (TO_2) and the other almost longitudinal (LO), and the corresponding frequencies can be written as

$$\begin{aligned} \omega_{\mathrm{TO}_2}^2(\theta) &= \beta\cos^2\theta + \alpha\sin^2\theta\,, \\ \omega_{\mathrm{LO}}^2(\theta) &= \tilde\omega_{\mathrm{pi}}^2 + \beta\sin^2\theta + \alpha\cos^2\theta\,. \end{aligned} \tag{32}$$

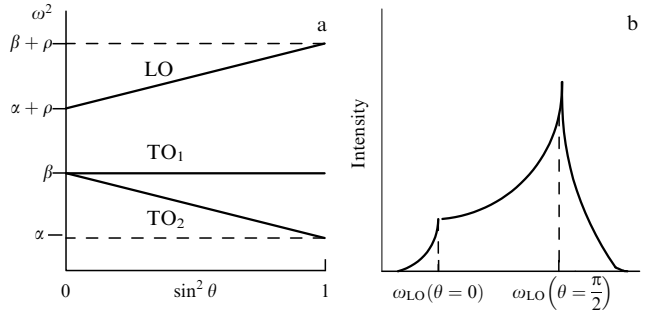

Figure 14. (a) Optical mode frequency in a uniaxial crystal as a function of the angle θ between the direction of the wave vector **k** and the principal c-axis. The TO_1 mode is polarized orthogonally to the c-**k** plane. The LO mode is longitudinal and the TO_2 mode transverse only when the effect of crystal anisotropy is small in comparison with the Coulomb interaction. (b) Effect of angular dispersion on the Raman line profile of the LO mode in a uniaxial crystal.

The angular dependences of frequency (32) are plotted in Fig. 14a, where $\rho=\tilde{\omega}_{pi}^2$; the dependences of this form (with constant ρ) were first proposed by Loudon [57]. Figure 14b shows the Raman line for a wide aperture of the incident laser beam; the line asymmetry is caused by angular dispersion.

We note that $\tilde{\omega}_{pi}^2$ in expression (32) also depends on the angle. However, the anisotropy of the inner shells' polarizability may prove to be smaller than the crystalline anisotropy responsible for the difference between α and β. There then exists a conservation law, specifically, the sum of the squared yz-mode frequencies is direction-independent. For instance,

$$\omega_{TO_2}^2(\theta=0)+\omega_{LO}^2(\theta=0) = \omega_{TO_2}^2\left(\theta=\frac{\pi}{2}\right)+\omega_{LO}^2\left(\theta=\frac{\pi}{2}\right). \quad (33)$$

To verify this law, one can take the example of the 6*H*-SiC polytype, where the angular dependence of optical frequencies is known from experiments [58, 55]. In the propagation along the crystal axis ($\theta=0$), the TO_2 and TO_1 modes are degenerate and their frequencies are equal to $\sqrt{\beta}$. The experimental frequency for the 6*H*-SiC polytype is 797 cm^{-1} (with an uncertainty of about 1 cm^{-1}). The corresponding frequency of the longitudinal mode is $\omega_{LO}(\theta=0)=(\omega_{pi}^2+\alpha)^{1/2}$. For the propagation perpendicular to the axis ($\theta=\pi/2$), $\omega_{TO_2}(\pi/2)=\sqrt{\alpha}$ (the experimental value is 788 cm^{-1}) and $\omega_{LO}(\theta=\pi/2)=(\omega_{pi}^2+\beta)^{1/2}$ (experiment gives a value of 970 cm^{-1}). Hence, it follows that $\omega_{pi}=552.9$ cm^{-1}, $\alpha=788^2$ cm^{-2}, $\beta=797^2$ cm^{-2}, and lastly $\omega_{LO}(\theta=0)=(\omega_{pi}^2+\alpha)^{1/2}=962.6$ cm^{-1}, which coincides with the experimental value, to within the experimental error.

5. Influence of charge carriers on phonon dispersion and damping

The problem of the interaction between phonons and conduction electrons is of fundamental importance in different areas of solid-state physics and above all in superconductivity. This is the reason why it invariably attracts the attention of theorists. The effect of free carriers on longitudinal optical phonons in semiconductors [59] and metals [60, 61] has been observed in experiments (see the review [62] and the recent paper [63] written on the high-temperature $Nd_{1.86}Ce_{0.14}CuO_{4+\delta}$ superconductor employing inelastic X-ray scattering). This effect is easy to explain because the longitudinal vibrations, for instance, in a polar dielectric, are accompanied by an electric field, which interacts with the carriers. This interaction is long-range in nature. It is sometimes referred to as the Coulomb screening and is described by the Maxwell equations.

At the same time, phonon vibrations are accompanied by a lattice deformation, and in the long-wavelength approximation they should be responsible for a change in the local electronic spectrum $\varepsilon(\mathbf{p},\mathbf{r},t)$. Two types of the corresponding deformation interaction are known. For acoustic branches this is the Fröhlich interaction. In the long-wavelength limit, acoustic deformation reduces to a simple shift, which should have no effect on the electrons. This interaction may contain only the derivatives of the displacement, i.e., the deformation tensor ε_{ij}:

$$\varepsilon(\mathbf{p},\mathbf{r},t)=\varepsilon_0(\mathbf{p})+\zeta_{ij}(\mathbf{p})\,\varepsilon_{ij}(\mathbf{r},t)\,.$$

For a cubic crystal it assumes the form

$$\varepsilon(\mathbf{p},\mathbf{r},t)=\varepsilon_0(\mathbf{p})+\zeta(\mathbf{p})\,\mathrm{div}\,\mathbf{u}(\mathbf{r},t)\,, \quad (34)$$

where $\zeta(\mathbf{p})$ is a scalar function of electron momentum.

The local deformation interaction in the form

$$\varepsilon(\mathbf{p},\mathbf{r},t)=\varepsilon_0(\mathbf{p})+\zeta_i(\mathbf{p})\,u_i(\mathbf{r},t) \quad (35)$$

is possible for optical phonons, where the coupling constant $\zeta_i(\mathbf{p})$ is a vector function.

The significant distinction between these two is that only the longitudinal phonon mode interacts with electrons in the case (34). Moreover, they differ by symmetry: in the former case, the phonon representation under consideration should allow a tensor function and, in the latter case, a vector function to exist.

Employing the diagram technique, A B Migdal arrived at the conclusion [64] (see also Ref. [65]) that the Fröhlich interaction results in a significant renormalization of the phonon spectrum. Namely, the acoustic phonon velocity should change by the order of magnitude $\tilde{s}=s(1-2\lambda)^{1/2}$, where $\lambda\sim\zeta^2$ is the dimensionless electron–phonon interaction constant. Hence, it is clear that the acoustic mode should be expected to soften significantly, while for $\lambda\to 1/2$ an instability even occurs. This result is inconsistent with the adiabaticity of the electron–phonon system. According to the Born–Oppenheimer approximation, light electrons should follow the relatively slow lattice vibrations and the variation of the phonon spectrum should therefore be small in the non-adiabaticity parameter $\sqrt{m/M}$, where m and M are the respective masses of electrons and ions. In the context of adiabatic approximation (see, for instance, Ref. [50]), the electron–phonon interaction (34), (35) itself arises only due to departures from adiabaticity. As shown by Brovman and Kagan [66], in the Hamiltonian of the system two terms appear that compensate each other in the calculation of phonon renormalizations so that the remaining contribution contains the non-adiabaticity parameter. Using one of the terms of the Fröhlich Hamiltonian type in the conventional diagram technique is therefore incorrect.

At the same time, a large number of papers are dedicated to the calculation of sound damping in metals on the basis of the kinetic equation (see review [67]), which represents the

electron–phonon renormalization directly. The effect of electron–phonon interaction was shown to be rather small to the extent of the non-adiabaticity parameter. Specifically, the change in the sound velocity $\delta s = \tilde{s} - s$ and the damping Γ for the phonon with a wave vector k and a frequency $\omega_k = sk$ are given by the formula

$$\frac{\delta s}{s} - \mathrm{i}\,\frac{\Gamma}{\omega_k} = \lambda \begin{cases} \dfrac{s^2}{v_\mathrm{F}^2} - \mathrm{i}\,\dfrac{\pi s}{2v_\mathrm{F}}\,, & kv_\mathrm{F} > |\omega_k + \mathrm{i}\tau^{-1}|\,, \\ \dfrac{\omega_k}{\omega_k + \mathrm{i}\tau^{-1}}\,, & kv_\mathrm{F} < |\omega_k + \mathrm{i}\tau^{-1}|\,, \end{cases} \tag{36}$$

where τ is the electron relaxation time and v_F is the Fermi velocity. We note that the non-adiabaticity parameter $s/v_\mathrm{F} \sim \sqrt{m/M}$ appears explicitly in the first of formulas (36) and appears in the second one when taking into account the domain of applicability.

The electron–phonon coupling constant λ is proportional to the state density on the Fermi surface $\nu_0 \sim m^* p_\mathrm{F}/\pi^2$ and the square of the deformation potential ζ_{ik}. The requirement that the number of electrons must be conserved upon the inclusion of electron–phonon interaction implies that λ vanishes in the isotropic case, and therefore Migdal should have obtained the zero result when considering the isotropic case.

Major renormalizations (in particular, extremely strong dispersion — on the order of the Fermi velocity) was predicted for optical phonons as well [68–70]. In a recent paper M Reizer [71] somewhat improved the situation by considering the screening of the long-range electric field emerging in longitudinal optical vibrations (it is likely that the effect of Coulomb screening on optical phonons was first noted in Ref. [72]; see also Ref. [73]). The strong dispersion disappeared, but the electron–phonon interaction was incorporated into the result in a non-physical way.

Extremely strong optical phonon dispersion has not been experimentally observed until the present time. Dedicated searches in osmium [74] in the long-wavelength range $kv_\mathrm{F} < |\omega + \mathrm{i}\tau^{-1}|$, where it should be observable according to Refs [68–70], yield the usual values of dispersion $\mathrm{d}\omega/\mathrm{d}k \sim 10^6$ cm s^{-1} for a Fermi velocity $v_\mathrm{F} = (3-5) \times 10^7$ cm s^{-1}. Experimentally, coupled phonon–plasmon modes in doped semiconductors supposedly furnish a good opportunity for investigating electron–phonon interactions. Two such modes $\mathrm{L}^{\pm}$ were repeatedly observed in experiments on Raman scattering (see, for instance, Ref. [75]). However, in the interpretation of experimental data advantage was always taken of the theory which included only the Coulomb screening; the effect of deformation (Fröhlich) interaction was neglected.

Here, we give the theoretical results [76] obtained with the inclusion of screening, deformation interaction, and the electron and phonon relaxation times. It is pertinent to note that the screening is determined by the dielectric function $\varepsilon(k, \omega)$. When comparing experimental data with theory, advantage is commonly taken of either the Drude form of conductivity or the so-called Lindhard–Mermin approximation [77], which is a rather artificial generalization of the Lindhard formula to the case of electron collisions. Applying the Lindhard formula is meaningful when the transferred wave vector k is comparable with the electron Fermi momentum p_F. The electron–phonon interaction is most pronounced in heavily doped semiconductors with a high density of carriers, which are degenerate under these conditions even at room temperature. The most appreciable effect occurs for $kv_\mathrm{F} \sim \omega$, where v_F is the Fermi velocity and ω is the phonon frequency, and usually the condition $k \ll p_\mathrm{F}$ is fulfilled in the studies of Raman scattering on samples with a carrier density of more than 10^{17} cm^{-3}. This condition allows us to consistently use the kinetic equation method in lieu of the Lindhard–Mermin approximation.

6. Raman scattering by interacting electrons and phonons

To take into account the conduction electrons and the electric field $\mathbf{E}(\mathbf{r}, t)$ excited in lattice oscillations we write the effective Hamiltonian (10) describing Raman scattering in the general form

$$\mathcal{H} = \frac{e^2}{mc^2} \int \mathrm{d}^3 r\, \mathcal{N}(\mathbf{r}, t)\, U(\mathbf{r}, t)\,, \tag{37}$$

where $U(\mathbf{r}, t)$ denotes the product of the vector potentials of the incident and scattered light:

$$A^{(\mathrm{i})}(\mathbf{r}, t) A^{(\mathrm{s})}(\mathbf{r}, t) = U(\mathbf{r}, t) = \exp\left[\mathrm{i}(\mathbf{kr} - \omega t)\right] U(\mathbf{k}, \omega)\,,$$

$\mathbf{k} = \mathbf{k}^{(\mathrm{i})} - \mathbf{k}^{(\mathrm{s})}$, $\omega = \omega^{(\mathrm{i})} - \omega^{(\mathrm{s})}$ are the transferred momentum and frequency, respectively.

The operator

$$\mathcal{N}(\mathbf{r}, t) = \gamma \hat{n}(\mathbf{r}, t) + g_j\, \hat{u}_j(\mathbf{r}, t) + g_E E(\mathbf{r}, t) \tag{38}$$

is linear in the electron number $\hat{n}$, phonon displacement $\hat{u}_j$, and field E operators. The polarizations of the vectors $\hat{\mathbf{u}}_j(\mathbf{r}, t)$, $\mathbf{E}(\mathbf{r}, t)$, $\mathbf{A}^{(\mathrm{i})}(\mathbf{r}, t)$, and $\mathbf{A}^{(\mathrm{s})}(\mathbf{r}, t)$ are included in the coupling constants. For instance, the vertex describing the light scattering with electron–hole pair production with the inclusion of possible resonance electron transitions between the band states in the second order of the perturbation theory has the form

$$\gamma(\mathbf{p}) = e_\alpha^{(\mathrm{i})} e_\beta^{(\mathrm{s})} \left[\delta_{\alpha\beta} + \frac{1}{m} \sum_n \left(\frac{p_{fn}^\beta p_{nf}^\alpha}{\epsilon_f(\mathbf{p}) - \epsilon_n(\mathbf{p}) + \omega^{(\mathrm{i})}} + \frac{p_{fn}^\beta p_{nf}^\alpha}{\epsilon_f(\mathbf{p}) - \epsilon_n(\mathbf{p}) - \omega^{(\mathrm{s})}} \right) \right].$$

In the quasiclassical approximation, the electron density fluctuations

$$\langle\langle \gamma \hat{n}(\mathbf{r}, t) \rangle\rangle = \int \frac{\mathrm{d}^3 p}{(2\pi)^3}\, \gamma(\mathbf{p}) f_\mathrm{p}(\mathbf{r}, t)\,, \tag{39}$$

averaged quantum-mechanically and statistically, are calculated employing the electron distribution function $f_\mathrm{p}(\mathbf{r}, t)$. It is easy to obtain an estimate of the deformation-optical and electrooptical vertices $g_j \sim 1/a^4$, $g_E \sim 1/ea$, as well as of the electron vertex $\gamma(\mathbf{p}) \sim m/m^*$, where a is the lattice constant and m^* is the effective electron mass.

The quantity $U(\mathbf{r}, t)$ can be considered as an external force, and it is possible to define the generalized susceptibility in the linear response to this force:

$$\langle\langle \mathcal{N}(\mathbf{k}, \omega) \rangle\rangle = -\chi(\mathbf{k}, \omega) U(\mathbf{k}, \omega)\,. \tag{40}$$

Next, with the aid of the fluctuation-dissipation theorem it is possible to write the equation

$$K(\mathbf{k},\omega)=\frac{2}{1-\exp\left(-\omega/T\right)}\,\mathrm{Im}\,\chi(\mathbf{k},\omega) \tag{41}$$

relating the susceptibility to the Fourier component of the correlation function

$$K(\mathbf{r},t;\mathbf{r}',t')=\langle\langle\mathcal{N}^{\dagger}(\mathbf{r},t)\,\mathcal{N}(\mathbf{r}',t')\rangle\rangle\,, \tag{42}$$

which depends on $\mathbf{r}-\mathbf{r}'$ and $t-t'$ by virtue of uniformity.

The Raman cross section is given by the formula

$$\frac{\mathrm{d}\sigma}{\mathrm{d}\omega^{(\mathrm{s})}\,\mathrm{d}\Omega^{(\mathrm{s})}}=\frac{k_z^{(\mathrm{s})}\omega^{(\mathrm{s})}}{\pi c}\left(\frac{2e^2}{c\hbar m\omega^{(\mathrm{i})}}\right)^2 K(\mathbf{k},\omega)\left|U(\mathbf{k},\omega)\right|^2, \tag{43}$$

where $k_z^{(\mathrm{s})}$ is the normal component of the wave vector [dependent on the parallel component and the frequency $\omega^{(\mathrm{s})}$] in the scattered wave. We do not enlarge here on surface effects related to the electron reflection from the surface of the sample (see Refs [78, 79]). The skin effect for the incident and scattered fields can be included by integrating $|U(\mathbf{k},\omega)|^2$ with respect to the normal component k_z, which gives the factor $1/\mathrm{Im}(k_z^{(\mathrm{i})}+k_z^{(\mathrm{s})})$. The resultant cross section proves to be dimensionless and gives the fraction of inelastic-scattered light relative to the incident beam intensity.

Therefore, the problem reduces to the determination of generalized susceptibility. To solve it, we can conveniently take advantage of the Boltzmann equation. In accordance with the concept of adiabatic approximation, the zero-approximation function $f_0[\varepsilon(\mathbf{p},\mathbf{r},t)-\mu]$ should be considered as depending on the local electronic spectrum:

$$\varepsilon(\mathbf{p},\mathbf{r},t)=\varepsilon_0(\mathbf{p})+\zeta_j(\mathbf{p})u_j(\mathbf{r},t)+\gamma(\mathbf{p})U(\mathbf{r},t)\,.$$

Here, the interaction with electrons was employed in the form of expression (35) and account was taken of the terms (37) and (38); the interaction (34) was considered in detail in Ref. [80].

From the electron number conservation condition we find the variation of the chemical potential

$$\mu=\mu_0+\langle\gamma(\mathbf{p})\rangle U(\mathbf{r},t)+\langle\zeta_j(\mathbf{p})\rangle b_j(\mathbf{r},t)\,,$$

which reduces to the renormalization of vertices

$$\gamma(\mathbf{p})\to\gamma(\mathbf{p})-\langle\gamma(\mathbf{p})\rangle\,,\qquad \zeta_j(\mathbf{p})\to\zeta_j(\mathbf{p})-\langle\zeta_j(\mathbf{p})\rangle\,. \tag{44}$$

The angular brackets denote integration over the Fermi surface,

$$\langle\ldots\rangle=\frac{1}{v_0}\int(\ldots)\frac{2\,\mathrm{d}S_{\mathrm{F}}}{v(2\pi)^3}\,,$$

the integration being normalized to the density of states so as to satisfy the condition $\langle 1\rangle=1$.

For the addition to the electron distribution function

$$f_{\mathrm{p}}(\mathbf{r},t)-f_0\left[\varepsilon(\mathbf{p},\mathbf{r},t)-\mu\right]=-\frac{\mathrm{d}f_0}{\mathrm{d}\varepsilon}\,\delta f_{\mathrm{p}}(\mathbf{r},t) \tag{45}$$

we obtain the equation of the Fourier-component form

$$\begin{aligned}&-\mathrm{i}(\omega-\mathbf{kv})\,\delta f_{\mathrm{p}}(\mathbf{k},\omega)\\&\quad=\psi_{\mathrm{p}}(\mathbf{k},\omega)-\frac{1}{\tau}\left[\delta f_{\mathrm{p}}(\mathbf{k},\omega)-\langle\delta f_{\mathrm{p}}(\mathbf{k},\omega)\rangle\right],\end{aligned} \tag{46}$$

where

$$\psi_{\mathrm{p}}(\mathbf{k},\omega)=e\mathbf{v}\mathbf{E}(\mathbf{k},\omega)-\mathrm{i}\omega\left[\zeta_j(\mathbf{p})\,u_j(\mathbf{k},\omega)+\gamma(\mathbf{p})U(\mathbf{k},\omega)\right].$$

Here, the time derivative of the electron energy variation enters in response to different factors: the Coulomb field, the deformation interaction (35), and the interactions (37) and (38), which describe Raman scattering. The collision integral is written in the τ approximation so that the continuity equation for the electron charge is fulfilled. The relaxation time τ is defined by electron – phonon collisions, defects, etc.; the methods of its calculation are well known [81, 82].

The phonon interaction with electrons and the field $U(\mathbf{r},t)$ manifests itself also in the equation of phonon motion:

$$\begin{aligned}(\omega_k^2-\omega^2)\,u_j(\mathbf{k},\omega)&=\frac{Z}{M'}\,E_j(\mathbf{k},\omega)-\frac{gU(\mathbf{k},\omega)}{M'N}\\&\quad-\frac{1}{M'N}\int\frac{2\,\mathrm{d}^3p}{(2\pi)^3}\,\zeta_j(\mathbf{p})\,\delta f_{\mathrm{p}}(\mathbf{k},\omega)\,,\end{aligned} \tag{47}$$

in which there enter the mean value of displacement $u_j(\mathbf{k},\omega)$, the reduced elementary cell mass M', and the number of elementary cells per unit volume N. The last term on the right-hand side of formula (47) is the derivative of the Hamiltonian with respect to the displacement u_j. For the interaction (34) this term is replaced with

$$+\frac{\mathrm{i}k_j}{M'N}\int\frac{2\mathrm{d}^3p}{(2\pi)^3}\zeta(\mathbf{p})\,\delta f_{\mathrm{p}}(\mathbf{k},\omega)\,.$$

The natural width can be taken into account by performing the change $\omega_k^2\to\omega_k^2-\mathrm{i}\omega\Gamma^{\mathrm{nat}}$ in the final results.

Since we aim to study the effect of carriers, the phonon frequency ω_k is assumed to be known, which should be calculated in the absence of the electric field E, disregarding all non-adiabatic corrections. In the long-wavelength approximation it can be written as $\omega_k^2=\omega_0^2\pm s^2k^2$, where s is on the order of the conventional sound velocity in metals and the sign corresponds to either the maximum or the minimum of the phonon branch.

The field $\mathbf{E}$, which describes the electron – phonon interaction, is given by the Maxwell equation (27), whence it is clear that it is longitudinal and defined by the longitudinal polarization component.

In order to avoid linking between the longitudinal and transverse modes, the transferred wave vector is assumed to be directed along the crystal symmetry axis, which is taken to be the z-axis. The equation $\mathrm{div}\,\mathbf{D}=0$ in the Fourier component form is $D_z(\mathbf{k},\omega)=0$, i.e.,

$$\begin{aligned}&\varepsilon_\infty E(\mathbf{k},\omega)+4\pi NZu_z(\mathbf{k},\omega)\\&\quad+\frac{4\pi\mathrm{i}e}{k}\int\frac{2\,\mathrm{d}^3p}{(2\pi)^3}\,\delta f_{\mathrm{p}}(\mathbf{k},\omega)-4\pi g_EU(\mathbf{k},\omega)=0\,,\end{aligned} \tag{48}$$

where the first term describes the contribution of the filled electronic states, the second the contribution of phonon vibrations to the polarization, the third (P_{e}) the contribution of charge carriers with the density $\rho=-\mathrm{div}\,\mathbf{P}_{\mathrm{e}}$, and the last one the contribution of the field $U(\mathbf{r},t)$ defined, according to the general rule, by differentiation of the Hamiltonian (37), (38): $P=-\partial\mathcal{H}/\partial E=-g_EU$.

Equations (46) – (48) make up a complete system of equations for the problem under consideration. Using the

solution of the kinetic equation, it is possible to bring the equation of phonon motion (47) and the Poisson equation (48) to the form

$$(\tilde{\omega}_j^2 - \omega^2)\, u_j(\mathbf{k},\omega) - \frac{\tilde{Z}}{M'}\, E_j(\mathbf{k},\omega) = -\frac{\tilde{g}_j U(\mathbf{k},\omega)}{M'N}\,, \qquad (49)$$

$$\varepsilon_e(\mathbf{k},\omega)E(\mathbf{k},\omega) + 4\pi N\bar{Z}u_z(\mathbf{k},\omega) = 4\pi\tilde{g}_E U(\mathbf{k},\omega)\,. \qquad (50)$$

The dielectric function of the electron system is found to be

$$\varepsilon_e(\mathbf{k},\omega) = \varepsilon_\infty + \varepsilon_\infty \frac{k_0^2}{k^2}\left[1 - \frac{\langle\omega/\Delta_p\rangle}{1 - \langle \mathrm{i}/\Delta_p\rangle/\tau}\right], \qquad (51)$$

where $\Delta_p = \omega - kv_z + \mathrm{i}\tau^{-1}$ and $k_0^2 = 4\pi e^2 \nu_0/\varepsilon_\infty$ is the Thomas–Fermi screening parameter. The phonon frequency, the effective ion charge, and the vertexes, all being renormalized by the deformation interaction, are defined by the expressions

$$\tilde{\omega}_j^2 = \omega_k^2 + \frac{\omega\nu_0}{M'N}\left(\left\langle\frac{\zeta_j^2(\mathbf{p})}{\Delta_p}\right\rangle + \frac{\mathrm{i}\langle\zeta_j(\mathbf{p})/\Delta_p\rangle^2}{\tau - \langle\mathrm{i}/\Delta_p\rangle}\right), \qquad (52)$$

$$\tilde{Z} = Z - \frac{\mathrm{i}e\nu_0}{N}\left(\left\langle\frac{v_z\zeta_j(\mathbf{p})}{\Delta_p}\right\rangle + \frac{\mathrm{i}\langle v_z/\Delta_p\rangle\langle\zeta_z(\mathbf{p})/\Delta_p\rangle}{\tau - \langle\mathrm{i}/\Delta_p\rangle}\right), \qquad (53)$$

$$\tilde{g}_j = g_j + \omega\nu_0\left(\left\langle\frac{\zeta_j(\mathbf{p})\gamma(\mathbf{p})}{\Delta_p}\right\rangle + \frac{\mathrm{i}\langle\zeta_j(\mathbf{p})/\Delta_p\rangle\langle\gamma(\mathbf{p})/\Delta_p\rangle}{\tau - \langle\mathrm{i}/\Delta_p\rangle}\right), \qquad (54)$$

$$\tilde{g}_E = g_E - \mathrm{i}e\nu_0\left(\left\langle\frac{v_z\gamma(\mathbf{p})}{\Delta_p}\right\rangle + \frac{\mathrm{i}\langle v_z/\Delta_p\rangle\langle\gamma(\mathbf{p})/\Delta_p\rangle}{\tau - \langle\mathrm{i}/\Delta_p\rangle}\right), \qquad (55)$$

and the charge $\bar{Z}$ differs from $\tilde{Z}$ (53) by the sign of the term that gives the renormalization. Equation (49) can be applied both to longitudinal and transverse phonons. In the latter case, the field should be put equal to zero, $E = 0$.

The following expression results for the susceptibility:

$$\chi(\mathbf{k},\omega) = \chi_e(\mathbf{k},\omega) + \frac{\tilde{g}_j^2\varepsilon_e(\mathbf{k},\omega)/NM' - 4\pi\tilde{g}_E\bar{g}_E(\tilde{\omega}_j^2 - \omega^2) - 4\pi\tilde{g}_j(\tilde{g}_E\tilde{Z} + \bar{g}_E\bar{Z})/M'}{(\tilde{\omega}_j^2 - \omega^2)\,\varepsilon_e(\mathbf{k},\omega) + 4\pi N\tilde{Z}\bar{Z}/M'}\,, \qquad (56)$$

where

$$\chi_e(\mathbf{k},\omega) = -\omega\nu_0\left(\left\langle\frac{\gamma^2(\mathbf{p})}{\Delta_p}\right\rangle + \frac{\mathrm{i}\langle\gamma(\mathbf{p})/\Delta_p\rangle^2}{\tau - \langle\mathrm{i}/\Delta_p\rangle}\right),$$

and $\bar{g}_E$ differs from $\tilde{g}_E$ (55) by the sign of the second term.

6.1 Electron Raman scattering

Formulas (41), (43), and (56) describe Raman scattering with the production of different excitations in the electron–phonon system. If we put $\tilde{g}_j = g_E = \tilde{Z} = \bar{Z} = 0$, we arrive at the scattering with the excitation of electron–hole pairs,

$$\chi(\mathbf{k},\omega) = \chi_e(\mathbf{k},\omega) + \frac{4\pi\tilde{g}_E^2}{\varepsilon_e(\mathbf{k},\omega)}\,, \qquad (57)$$

with only the term in parenthesis to be kept in the expression for $\tilde{g}_E$ (55). For an arbitrary electronic spectrum, expression (57) can be calculated in the limits of large and small values of the parameter $\kappa = kv_F/(\omega + \mathrm{i}\tau^{-1})$. For $|\kappa| \gg 1$, formula (51) gives

$$\varepsilon_e(\mathbf{k},\omega) = \varepsilon_\infty\left\{1 + \left(\frac{k_0}{k}\right)^2\left[1 + \mathrm{i}\,\frac{\pi\omega}{k}\left\langle\frac{\delta(\mu)}{v}\right\rangle\right]\right\}, \qquad (58)$$

where $\mu = \mathbf{vk}/vk$ and $\delta(x)$ is the Dirac function. Here, the imaginary part is called the Landau damping, and the corresponding Raman scattering

$$\mathrm{Im}\,\chi(\mathbf{k},\omega) = \frac{\pi\omega}{k}\left\langle\frac{\gamma^2(\mathbf{p})\delta(\mu)}{v}\right\rangle \qquad (59)$$

was first calculated for the case of superconductors in Ref. [83]. In the isotropic case, it vanishes [84] owing to condition (44).

In the opposite 'dirty' limiting case $|\kappa| \ll 1$ the first term in expression (57), which describes electron–hole pair production,

$$\mathrm{Im}\,\chi_e(\mathbf{k},\omega) = \langle\gamma^2(\mathbf{p})\rangle\,\frac{\omega\tau}{(\omega\tau)^2 + 1}\,, \qquad (60)$$

was obtained in Ref. [85] employing the Green function technique.

The second term in expression (57) gives the scattering with plasmon production. In this case, it is expedient to expand in k the dielectric function

$$\varepsilon_e(k,\omega) = \varepsilon_\infty\left(1 - \frac{\omega_{pe}^2 + k^2 w}{\omega(\omega + \mathrm{i}\tau^{-1})}\right), \qquad (61)$$

where the k-independent term is related to the Drude conductivity, the electron plasma frequency being given by the integral over the Fermi surface $\omega_{pe}^2 = k_0^2\langle v_z^2\rangle$. The complex coefficient

$$w = \frac{k_0^2\left(\langle v_z^4\rangle + \mathrm{i}\langle v_z^2\rangle^2/\omega\tau\right)}{(\omega + \mathrm{i}\tau^{-1})^2}$$

determines the plasmon dispersion. For a quadratic electronic spectrum, $\langle v_z^2\rangle = v_F^2/3$ and $\langle v_z^4\rangle = v_F^4/5$. Since we have put $g_E = 0$, the k-expansion of the vertex $\tilde{g}_E$ has the form

$$\tilde{g}_E = -\frac{\mathrm{i}e\nu_0 k\langle\gamma(\mathbf{p})v_z^2\rangle}{(\omega + \mathrm{i}\tau^{-1})^2}\,.$$

The plasmon peak intensity is therefore proportional to k^2 in accordance with the general requirements for the dynamic structure factor.

6.2 Raman scattering by transverse phonons

The cross section for the scattering by transverse phonons can be obtained by putting $\tilde{Z} = \bar{Z} = \tilde{g}_E = 0$ in expression (56):

$$\chi(\mathbf{k},\omega) = \frac{\tilde{g}_{TO}^2/NM'}{\tilde{\omega}_{TO}^2 - \omega^2 - \mathrm{i}\omega\Gamma^{nat}}\,. \qquad (62)$$

We separate the real and imaginary parts to rewrite this expression in the form

$$\mathrm{Im}\,\chi(\mathbf{k},\omega) = \frac{1}{NM'}\,\frac{\omega\Gamma g_{TO}^2 + \left[\mathrm{Re}\,\tilde{\omega}_{TO}^2 - \omega^2\right]\mathrm{Im}\,\tilde{g}_{TO}^2}{\left[\mathrm{Re}\,\tilde{\omega}_{TO}^2 - \omega^2\right]^2 + (\omega\Gamma)^2}\,, \qquad (63)$$

and $\tilde{\omega}_{TO}$, $\tilde{g}_{TO}$ are given by expressions (52) and (54). We find the shift and width of the resonance curve

$$\Delta\omega_k = \mathrm{Re}\,\frac{\tilde{\omega}_{TO}^2 - \omega_k^2}{2\omega_k}\,, \qquad \Gamma = \Gamma^{nat} - \mathrm{Im}\,\frac{\tilde{\omega}_{TO}^2}{\omega_k}$$

with the aid of expression (52), in which the vertex should correspond to a transverse phonon polarized, for definiteness, along the x-axis: $\zeta_j(\mathbf{p}) = \zeta_x(\mathbf{p})$. In the limiting case $\kappa \gg 1$ we obtain

$$\tilde{\omega}_{\mathrm{TO}}^2 = \omega_k^2 + \frac{v_0\omega_k}{k}\left\langle \zeta_x^2(\mathbf{p})\left(-\mathrm{i}\pi + \frac{2\omega_k}{kv}\right)\frac{\delta(\mu)}{v}\right\rangle, \qquad (64)$$

and for $\kappa \ll 1$,

$$\tilde{\omega}_{\mathrm{TO}}^2 = \omega_k^2 + \frac{\omega_k}{\omega_k + \mathrm{i}\tau^{-1}}\left(\left\langle\zeta_x^2(\mathbf{p})\right\rangle + \frac{k^2\left\langle v_z^2\zeta_x^2(\mathbf{p})\right\rangle}{(\omega_k + \mathrm{i}\tau^{-1})^2}\right). \qquad (65)$$

We emphasize that the frequency renormalization is defined by the density of states v_0 and the deviation of interaction from the average value $\zeta_x(\mathbf{p}) - \langle\zeta_x(\mathbf{p})\rangle$, which naturally vanishes in the isotropic case. One can see that the interaction broadens transverse phonons and makes them harder. The maximum relative renormalization is on the order of $\lambda a p_{\mathrm{F}} m^* \omega/m|\omega + \mathrm{i}\tau^{-1}|$ for $kv \sim |\omega + \mathrm{i}\tau^{-1}|$, where λ is the dimensionless electron – phonon coupling constant and m^* is the effective electron mass.

From expression (63) it also follows that the lineshape proves to be asymmetric in the presence of electron – phonon interaction, because there appears an imaginary part in $\tilde{g}_{\mathrm{TO}}$. This effect (the emergence of asymmetry of a narrow resonance on the strength of its interaction with a broad continuum) is referred to as the Fano resonance [86]. The limiting expressions for $\tilde{g}_{\mathrm{TO}}$ (54) are obtained from expressions (64) and (65) by way of the substitution $\zeta_x^2(\mathbf{p}) \to \zeta_x(\mathbf{p})\,\gamma(\mathbf{p})$.

6.3 Raman scattering by longitudinal phonon – plasmon modes

In a nonpolar crystal, the scattering by longitudinal phonons differs from the scattering by the transverse ones by only the change of the constant $g_{\mathrm{TO}} \to g_{\mathrm{LO}}$, and in a cubic crystal these constants are equal. In a polar crystal or a crystal with carriers there additionally appears in expression (56) the contribution of the generated Coulomb field with the constant g_E. The formula simplifies in the limit $k = 0$, when it follows from Eqns (53) and (55) that the effective charge and the electrooptical coefficient are not renormalized by the electron – phonon interaction: $\widetilde{Z} = \bar{Z} = Z$, $\tilde{g}_E = g_E$. The longitudinal phonon frequency $\tilde{\omega}_0$ (52) and the strain-optical constant $\tilde{g}_{\mathrm{LO}}$ (54) are renormalized; the corresponding limiting expressions are similar to formulas (64) and (65). The aforesaid concerning the TO-line symmetry also applies to the LO phonon.

Since the dielectric function of the electron – phonon system in the long-wavelength limit is

$$\varepsilon(0,\omega) = \varepsilon_{\mathrm{e}}(0,\omega) + \frac{4\pi NZ^2}{M'(\tilde{\omega}_0^2 - \mathrm{i}\omega\Gamma^{\mathrm{nat}} - \omega^2)}, \qquad (66)$$

the second term in formula (56) has poles under the condition $\varepsilon(0,\omega) = 0$, which defines the frequencies $\omega_\pm$ of coupled phonon – plasmon modes for $k = 0$. When the electron and phonon relaxation frequencies $\tau^{-1} = \Gamma^{\mathrm{nat}} = 0$ and the deformation potential $\zeta_{\mathrm{LO}}(\mathbf{p}) = 0$ the well-known formula for the frequencies

$$\omega_\pm^2 = \frac{1}{2}(\omega_{\mathrm{pe}}^2 + \omega_{\mathrm{LO}}^2) \pm \frac{1}{2}\left[(\omega_{\mathrm{pe}}^2 + \omega_{\mathrm{LO}}^2)^2 - 4\omega_{\mathrm{pe}}^2\omega_{\mathrm{TO}}^2\right]^{1/2} \qquad (67)$$

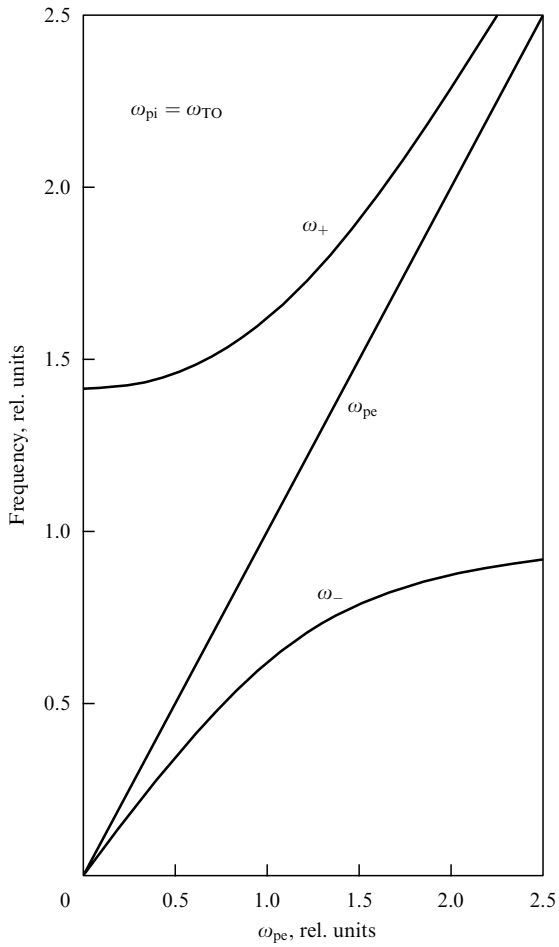

Figure 15. Dependence of the phonon – plasmon mode frequencies (in units of ω_{TO}) on the electron plasma frequency (in units of ω_{TO}), i.e., on the density of free electrons, for $k = 0$. The frequency ratio $\omega_{\mathrm{pi}} = \omega_{\mathrm{TO}}$ was selected, in this case $\omega_{\mathrm{LO}}/\omega_{\mathrm{TO}} = \sqrt{2}$.

results, where $\omega_{\mathrm{TO}} = \omega_k$ is the transverse-phonon frequency for $k = 0$, $\omega_{\mathrm{LO}}^2 = \omega_{\mathrm{TO}}^2 + \omega_{\mathrm{pi}}^2$, and $\omega_{\mathrm{pi}}^2 = 4\pi NZ^2/\varepsilon_\infty M'$.

The dependence of the frequencies $\omega_\pm$ on the carrier density, more precisely on $\omega_{\mathrm{pe}}/\omega_{\mathrm{TO}}$, is plotted in Fig. 15. The upper curve starts from ω_{LO} and tends to the electron plasma frequency ω_{pe}. The lower curve begins as $\omega_{\mathrm{pe}}\omega_{\mathrm{TO}}/\omega_{\mathrm{LO}}$ and approaches the value ω_{TO}. Therefore, by observing in the optical region the longitudinal mode and adding electrons we will notice the ω_{LO}-to-ω_{TO} frequency transition. This is the result of Coulomb screening.

In the long-wavelength limit, $k = 0$, the Raman scattering by longitudinal modes was calculated by Hon and Faust [87], disregarding both the electron – phonon deformation interaction and the relaxation processes. In this case, formula (56) can be rewritten as

$$\chi(0,\omega) = \frac{(4\pi g_E)^2}{\varepsilon_\infty\varepsilon(0,\omega)}\left[\frac{\varepsilon_{\mathrm{e}}(0,\omega)A^2\chi_I}{\varepsilon_\infty} - \frac{\varepsilon_\infty}{4\pi} - 2A\chi_I\right], \qquad (68)$$

where

$$\chi_I = \frac{NZ^2}{M'(\omega_{\mathrm{TO}}^2 - \mathrm{i}\omega\Gamma^{\mathrm{nat}} - \omega^2)}, \qquad A = \frac{C\omega_{\mathrm{TO}}^2 M'\varepsilon_\infty}{4\pi NZ^2},$$

and $C = g_{\mathrm{LO}}Z/g_E M\omega_{\mathrm{TO}}^2$ is the so-called Faust – Henry constant. Expression (68) coincides with the Hon – Faust formula [see, for instance, Ref. [88], Eqn (3.1)].

For $k \neq 0$, the coupled-mode frequencies are defined by the poles of expression (56), i.e., by the equation

$$(\tilde{\omega}_j^2 - \mathrm{i}\omega\Gamma^{\mathrm{nat}} - \omega^2)\,\varepsilon_{\mathrm{e}}(\mathbf{k},\omega) + \frac{4\pi N\tilde{Z}\bar{Z}}{M'} = 0 \tag{69}$$

with the renormalized phonon frequency and ion charge. The renormalization also appears in the numerator of expression (56). When the deformation interaction is absent, $\zeta_{\mathrm{LO}}(\mathbf{p}) = 0$, the effect of carriers manifests itself in the term $g_{\mathrm{LO}}\tilde{g}_E$ owing to the interference with the electronic scattering $\gamma(\mathbf{p})$.

The expansion of $\tilde{g}_E$ is of the form

$$\tilde{g}_E = g_E - \frac{\mathrm{i}ev_0k\langle v_z^2\gamma(\mathbf{p})\rangle}{(\omega + \mathrm{i}\tau^{-1})^2} \tag{70}$$

for $|\kappa| \ll 1$ and

$$\tilde{g}_E = g_E + ev_0k^{-2}(\omega + \mathrm{i}\tau^{-1})\left\langle\gamma(\mathbf{p})\left(-\frac{\pi}{2} - \frac{\mathrm{i}\omega}{kv}\right)\frac{\delta(\mu)}{v}\right\rangle \tag{71}$$

for $|\kappa| \gg 1$. We note that the imaginary part of $\tilde{g}_{\mathrm{LO}}\bar{g}_E$, which is responsible for the line asymmetry, is most pronounced when $\omega\tau \simeq 1$.

The dispersion of coupled modes is shown schematically in Fig. 16. We note its behavior for large k. One of the modes, which is primarily of a plasmon nature, asymptotically approaches the straight line $\omega = kv_{\mathrm{F}}$ for a low electron collision rate τ^{-1}. The reason lies with the singularity of the electron contribution (51) to the dielectric function

$$\varepsilon_{\mathrm{e}}(k,\omega) = \varepsilon_\infty + \varepsilon_\infty\frac{k_0^2}{k^2} \times\left\{1 - \frac{\omega}{2kv_{\mathrm{F}}}\left[\frac{1}{2}\ln\frac{4k^2v_{\mathrm{F}}^2}{(\omega - kv_{\mathrm{F}})^2 + \tau^{-2}} - \mathrm{i}\,\frac{\tau^{-1}}{\omega - kv_{\mathrm{F}}}\right]\right\} \tag{72}$$

for $\tau^{-1} < \omega - kv_{\mathrm{F}} \ll kv_{\mathrm{F}}$.

The other mode, which is of the phonon type, possesses a relatively weak dispersion. This mode penetrates into the $kv_{\mathrm{F}} \gg \omega$ range, and here its damping decreases with k. We will consider this mode in greater detail. The second term in formula (52), which defines the renormalized frequency $\tilde{\omega}_j$, is smaller than the first one both for small and large κ. Furthermore, we ignore the renormalization of the ion charge, which is weak in the limit of small $|\kappa| \ll 1$, and give

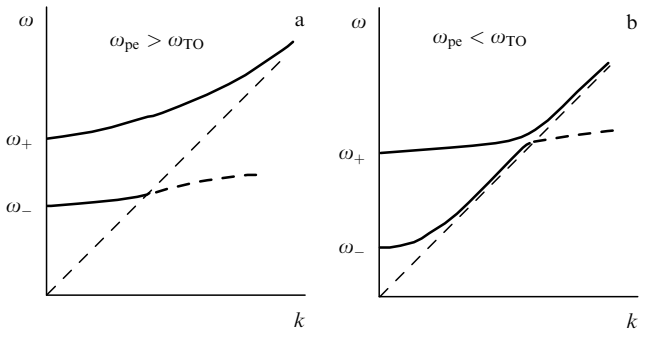

Figure 16. Dispersion of phonon–plasmon modes for 'metallic', $\omega_{\mathrm{pe}} > \omega_{\mathrm{TO}}$ (a), and semiconductor, $\omega_{\mathrm{pe}} < \omega_{\mathrm{TO}}$ (b) carrier densities. The dashed straight lines separate the $kv_{\mathrm{F}} > \omega$ domain, where the Landau damping exists, and the dashed curves in this domain depict the damping modes.

the solution of Eqn (69) for the frequency and damping of the phonon-type mode:

(i) low carrier density, $\omega_{\mathrm{pe}} < \omega_{\mathrm{TO}}$,

$$|\kappa| \ll 1\,,\quad \omega^2 = \omega_{\mathrm{LO}}^2 - \mathrm{i}\omega_{\mathrm{LO}}\Gamma^{\mathrm{nat}} + \frac{\lambda\omega_{\mathrm{LO}}\omega_{\mathrm{TO}}^2}{\omega^*}\left(1 + \frac{\kappa^2}{3}\right) + \frac{(\omega_{\mathrm{pi}}\omega_{\mathrm{pe}})^2}{\omega_{\mathrm{LO}}\omega^*}\left(1 + \frac{\mathrm{i}\kappa^2}{3\tau\omega_{\mathrm{LO}}}\right), \tag{73}$$

$$|\kappa| \gg 1\,,\quad \omega^2 = \omega_{\mathrm{LO}}^2 - \mathrm{i}\omega_{\mathrm{LO}}\Gamma^{\mathrm{nat}} + \frac{\lambda\omega_{\mathrm{LO}}\omega_{\mathrm{TO}}^2}{kv_{\mathrm{F}}}\left(-\mathrm{i}\,\frac{\pi}{2} + \frac{1}{\kappa}\right) - \frac{3(\omega_{\mathrm{pi}}\omega_{\mathrm{pe}})^2}{(kv_{\mathrm{F}})^2}\left(1 + \frac{\mathrm{i}\pi\omega_{\mathrm{LO}}}{2kv_{\mathrm{F}}}\right), \tag{74}$$

where $\omega^* = \omega_{\mathrm{LO}} + \mathrm{i}/\tau$.

(ii) high carrier density, $\omega_{\mathrm{pe}} \gg \omega_{\mathrm{TO}}$,

$$|\kappa| \ll 1\,,\quad \omega^2 = \omega_{\mathrm{TO}}^2 - \mathrm{i}\omega_{\mathrm{TO}}\Gamma^{\mathrm{nat}} + \frac{\lambda\omega_{\mathrm{TO}}^3}{\omega^*}\left(1 + \frac{\kappa^2}{3}\right) - \frac{\omega_{\mathrm{pi}}^2\omega_{\mathrm{TO}}\omega^*}{\omega_{\mathrm{pe}}^2}\left(1 - \frac{\mathrm{i}\kappa^2}{3\tau\omega_{\mathrm{TO}}}\right), \tag{75}$$

$$|\kappa| \gg 1\,,\quad \omega^2 = \omega_{\mathrm{TO}}^2 - \mathrm{i}\omega_{\mathrm{TO}}\Gamma^{\mathrm{nat}} + \frac{\lambda\omega_{\mathrm{TO}}^3}{kv_{\mathrm{F}}}\left(-\mathrm{i}\,\frac{\pi}{2} + \frac{1}{\kappa}\right) + \frac{(\omega_{\mathrm{pi}}kv_{\mathrm{F}})^2}{3\omega_{\mathrm{pe}}^2}\left(1 - \frac{\mathrm{i}\pi\omega_{\mathrm{TO}}}{2kv_{\mathrm{F}}}\right), \tag{76}$$

where $\omega^* = \omega_{\mathrm{TO}} + \mathrm{i}/\tau$. The definition of λ depends on κ:

$$\lambda = \frac{v_0\langle\zeta^2(\mathbf{p})\rangle}{M'N\omega_{\mathrm{TO}}^2}\,,\qquad \kappa \ll 1\,,$$

$$\lambda = \frac{v_0v_{\mathrm{F}}^2\langle\zeta^2(\mathbf{p})/v_z^2\rangle}{M'N\omega_{\mathrm{TO}}^2}\,,\qquad \kappa \gg 1\,.$$

The order of magnitude proves to be the same in both cases: $\lambda \sim p_{\mathrm{F}}am^*/m$.

The most significant effect of Coulomb interaction is screening, which reduces to the change of the first term $\omega_{\mathrm{LO}}^2 \to \omega_{\mathrm{TO}}^2$ on the right-hand sides of equalities (73)–(76) with an increase in carrier density. The last terms on the right-hand side, which do not contain λ, are a small correction in the screening. For instance, for a high carrier density [expressions (75), (76)] they are small in the parameter $\omega_{\mathrm{pi}}^2/\omega_{\mathrm{pe}}^2 \sim m/M$. Nevertheless, this correction is significant in expression (76), for it is responsible for dispersion. The dispersion parameter is the $v_{\mathrm{F}}\omega_{\mathrm{pi}}/\omega_{\mathrm{pe}}$ quantity, which is on the same order of magnitude as the sound velocity.

The terms with λ describe the effect of deformation interaction. We emphasize once again that these terms vanish in the isotropic case by virtue of the electron number conservation condition upon the inclusion of electron–phonon interaction (44). In the short-wavelength domain [expressions (74), (76)] they contain the non-adiabaticity parameter s/v_{F} explicitly, because the phonon frequencies $\omega \sim s/a$. In the long-wavelength domain [expressions (73), (75)], the non-adiabaticity parameter has an effect on the width of this domain itself: $k \ll |\omega + \mathrm{i}\tau^{-1}|/v_{\mathrm{F}}$. Here, the electron–phonon interaction effects become stronger as the Fermi surface departs from sphericity, as well as with an increase in carrier density and effective carrier mass; the last-named quantities enter into the definition of λ.

In the limiting cases of small and large κ, the frequency renormalization is given by the same integral over the Fermi

surface $\langle 1/\Delta_p(k)\rangle$ as the dielectric function $\varepsilon_e(k,\omega)$. For explicit calculations it is required to know the form of the electronic spectrum. As an interpolation to the intermediate values of κ, use can be made of the value of the integral calculated for an isotropic Fermi surface:

$$\left\langle 1/\Delta_p(k)\right\rangle = \frac{1}{2kv_F}\ln\frac{1+\kappa}{1-\kappa}, \qquad \kappa = \frac{kv_F}{\omega + i\tau^{-1}}, \tag{77}$$

where advantage is taken of that branch of $\ln x$ which is real for positive real values of x with a cut along negative x.

The results of numerical calculations are given in Figs 17–20. In this case, electron Raman scattering was ignored, $\gamma(\mathbf{p}) = 0$, and use was made of the typical value of the Faust–Henry constant $C = -0.5$ of electron and phonon relaxation [88, 89]: $\tau^{-1} = 10^{-1}\omega_{TO}$ and $\Gamma^{nat} = 10^{-2}\omega_{TO}$. The ion plasma frequency was assumed to be $\omega_{pi} = \omega_{TO}$, and therefore $\omega_{LO} = \sqrt{2}\omega_{TO}$. In Figs 17–20, the frequency ω is given in units of ω_{TO} and the wave vector k and the Thomas–Fermi parameter k_0 are given in units of ω_{TO}/v_F. Low and high carrier densities differ by the value of k_0; for a quadratic spectrum, the electron plasma frequency is $\omega_{pe} = k_0 v_F/\sqrt{3}$.

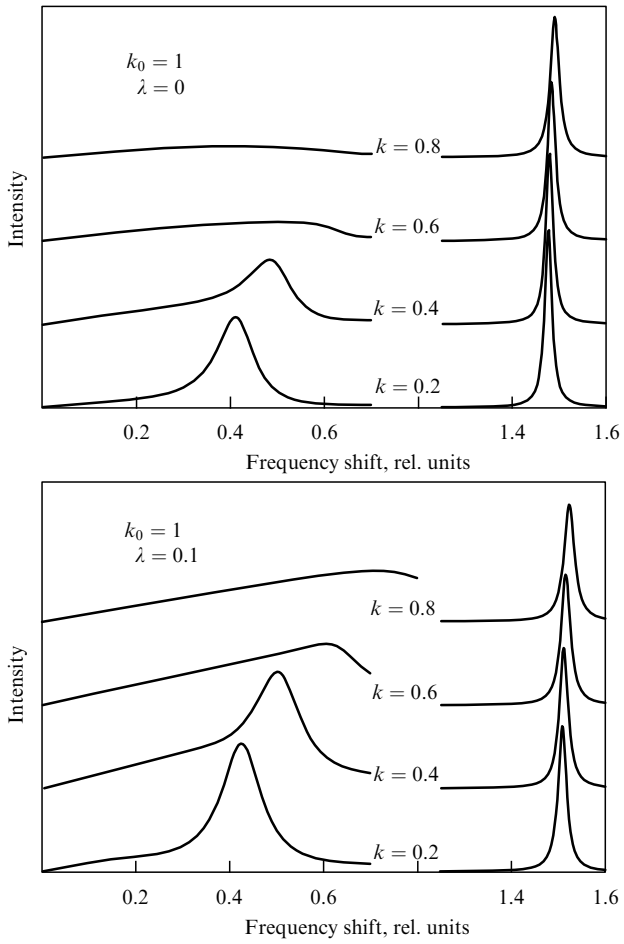

Figure 17. Raman spectra versus transferred frequency (in units of ω_{TO}) for a semiconductor with a low carrier density defined by the Thomas–Fermi parameter k_0 (in units of ω_{TO}/v_F) and for two values of the electron–phonon constant λ; the transferred momentum (in units of ω_{TO}/v_F) is specified in the curves. Chosen were the frequency ratio $\omega_{LO}/\omega_{TO} = \sqrt{2}$ and the width ratios $\Gamma^{nat}/\omega_{TO} = 10^{-2}$, $\tau^{-1}/\Gamma^{nat} = 10$. The right peak is primarily phonon in character and the left one is primarily plasmon in character.

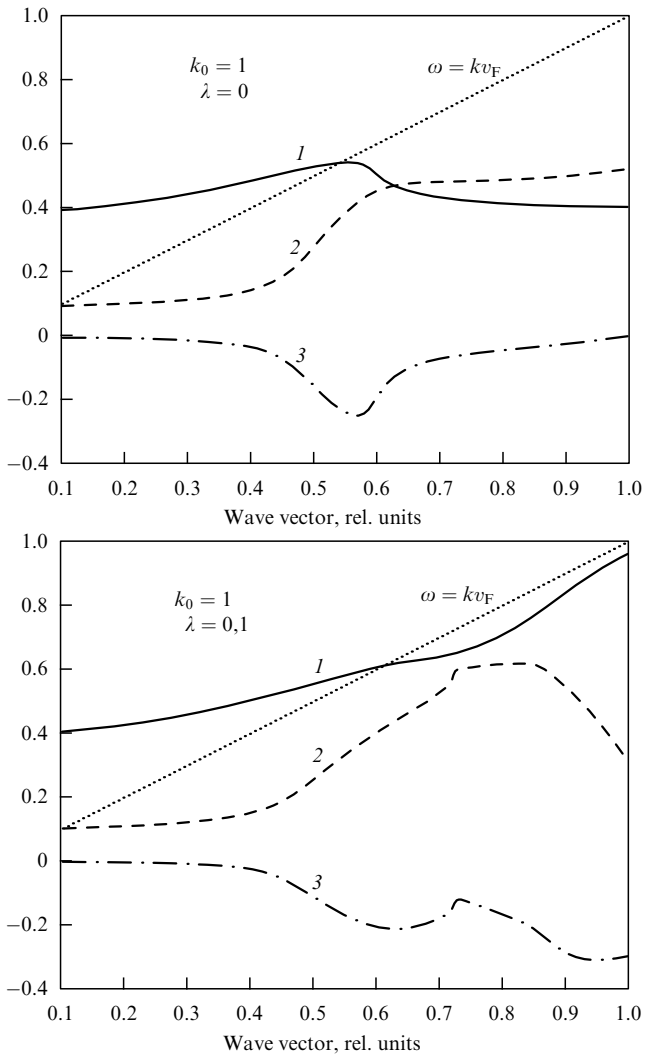

Figure 18. Dispersion (*1*), width (*2*), and asymmetry (*3*) (in units of ω_{TO}) of the plasmon peak (the left peak in Fig. 17) for a low carrier density. Landau damping exists in the domain to the right of the dotted straight line.

In Fig. 17, the left peak at $\omega/\omega_{TO} \sim 0.45$ depicts the plasmon-type vibration, while the right at $\omega \sim \omega_{LO} \sim 1.5\omega_{TO}$ corresponds to a primarily phonon-type vibration of significantly higher intensity (their relative amplitudes are not drawn to scale in Fig. 17). When the wave vector approaches the boundary of the domain $kv_F > \omega$, where the Landau damping arises (Fig. 16b), the plasmon peak broadens and nearly vanishes for $k = 0.8$. The plasmon peak intensity increases relative to the phonon peak intensity with an increase in the λ constant. The broad continuum for $\omega < kv_F$ emerges due to the excitation of electron–hole pairs.

The dispersion (i.e., the resonance frequency as a function of k, curve *1*), the half-width of the resonance curve (curve *2*), and the line asymmetry (the difference between the right and left abscissas corresponding to the half-height, curve *3*) are shown in Fig. 18 for the plasmon peak. All quantities are expressed in units of ω_{TO}. The width and the asymmetry increase significantly when the peak approaches the $kv_F > \omega$ domain. Figure 19 depicts the phonon peak behavior in the vicinity of $\omega = \omega_{LO}$. When k increases from 0 to 1.7, the phonon peak shifts toward higher frequencies and broadens — this is the effect of Landau

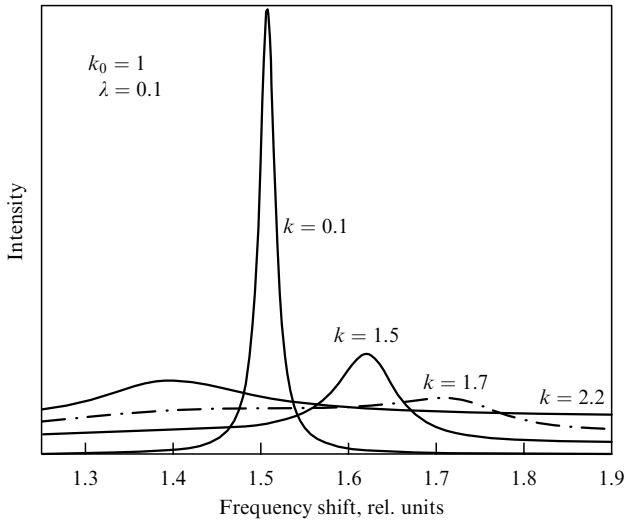

Figure 19. Phonon-type resonance for large transferred momenta.

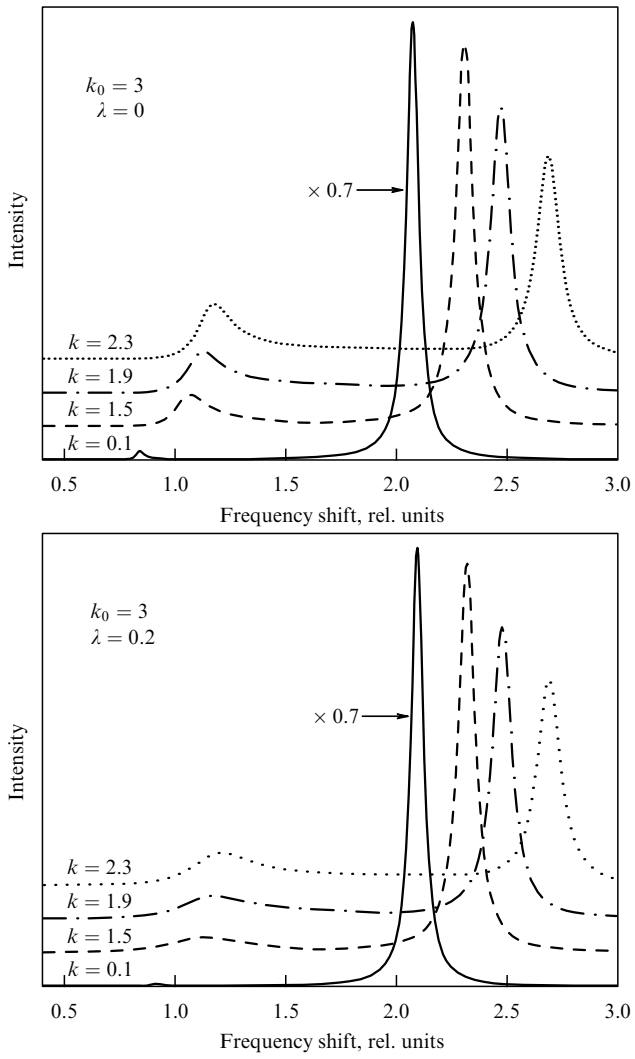

Figure 20. Raman spectra for a heavily doped sample. Here, the right peak is primarily of a plasmon nature and the left peak primarily of a phonon one.

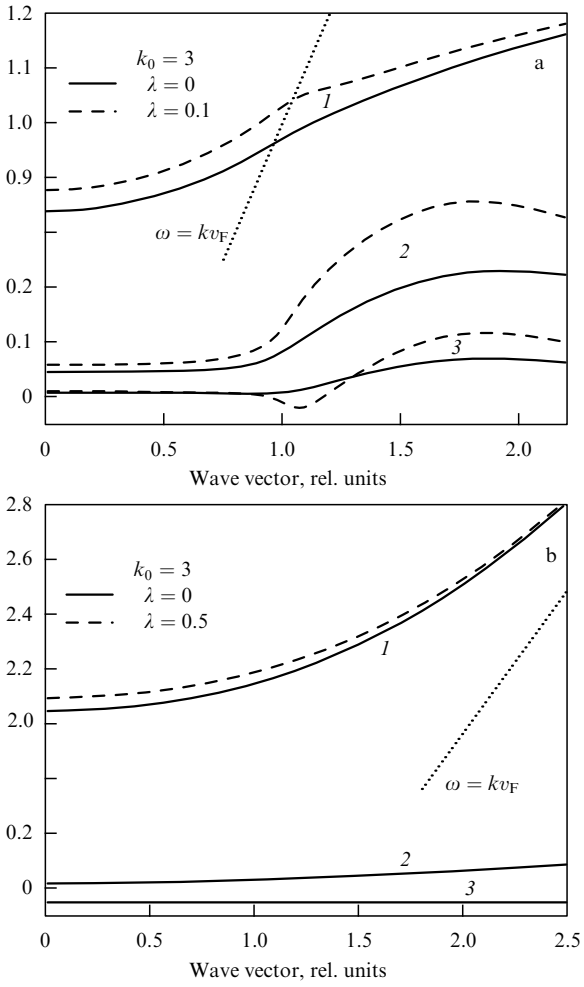

Figure 21. Dispersion (*1*), width (*2*), and asymmetry (*3*) (in units of ω_{TO}) of the phonon (a) and plasmon (b) peaks for a high carrier density.

damping (see Fig. 16). But for $k > 1.75$ the peak emerges on the lower-frequency side, $\omega \simeq 1.4$, and becomes narrower for $k > 2.2$, because Landau damping decreases with k [see expression (58)].

The Raman spectra calculated for heavily doped semiconductors and metals are given in Fig. 20. The longitudinal vibration, which is primarily of a phonon nature, is now excited approximately for $\omega/\omega_{TO} \sim 1$. The resonances are asymmetric. The corresponding dispersion dependences for the phonon and plasmon vibrations are plotted in Fig. 21. The feature for $k \simeq \omega/v_F$ is clearly visible.

6.4 Influence of the metal–insulator transition on the phonon spectrum

The effect of carriers on the phonon spectrum will be discussed by the striking example of a metal–dielectric transition occurring in a GaN compound under pressure. It is well known that GaN at a pressure of about 20 GPa experiences a transition from a metal state with a carrier number density of 5×10^{19} cm^{-3} to a semiconductor state with a carrier number density of 3×10^{18} cm^{-3}. In the semiconductor state, the crystal becomes transparent, the transition also being confirmed by photoluminescence data. The transition is attributed to the fact that the energy gap width increases with pressure, while the energy of the donor level related to the valence band remains invariable. At some

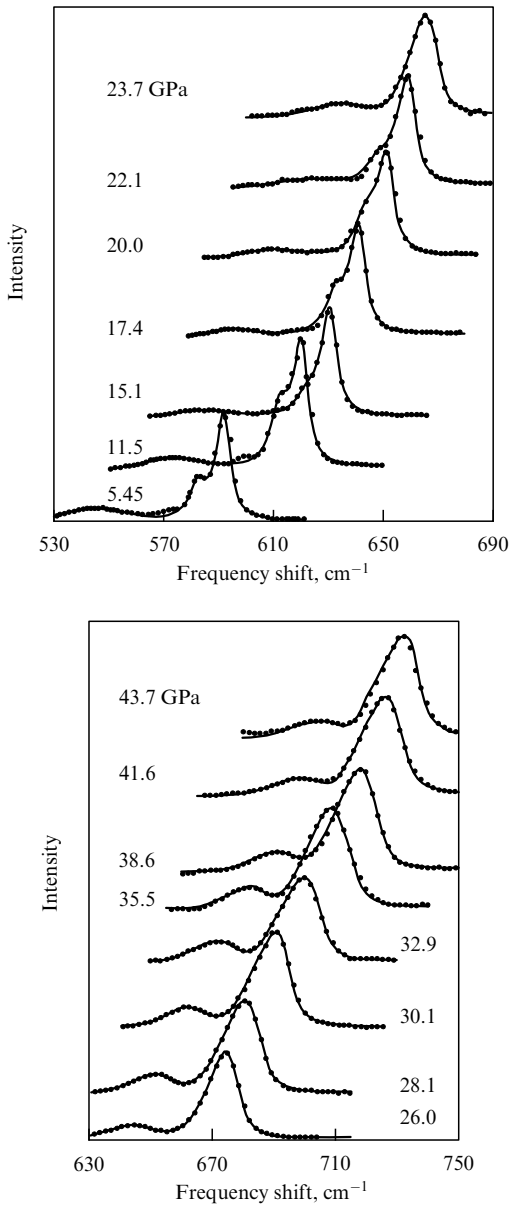

Figure 22. Raman spectra of a GaN monocrystal under pressure. Solid curves show the result of comparison with the theory, Eqns (15) – (17). One can see the splitting in the neighborhood of the E2 mode (580 – 600 cm^{-1} for $P = 5.45$ GPa). The width of the A1 mode (520 – 570 cm^{-1} for $P = 5.45$ GPa) is significantly greater owing to the interaction with carriers; in the semiconductor state (above 22 GPa) the width becomes smaller.

pressure this level is found to lie below the bottom of the conduction band.

The Raman spectra in the neighborhood of the most intense mode E2 recorded with a GaN monocrystal in a broad pressure range [90, 91] are shown in Fig. 22; the solid curves were plotted [92] with the aid of Eqns (15) – (17).

With increasing pressure, the splitting seen at normal pressure in the 568 cm^{-1} region (these are most likely the E2 and E1 modes) becomes unobservable; all modes shift toward higher frequencies; the widths increase monotonically for E2 and for the weak and broad A1 mode (530 cm^{-1} at normal pressure) everywhere, with the exception for the 20 – 30 GPa interval.

The hardening of phonon modes under uniform compression is a well-known phenomenon. It was observed, for instance, in a cubic 3*C*-SiC as well as in Si [8, 10]. However, the frequency shift in GaN is abnormally large — it amounts to 50% as pressure increases up to 44 GPa. Moreover, the linewidths also increase and lineshapes acquire an asymmetric form, testifying to the rise in the number of defects and to the inhomogeneity of stress in the sample under pressure.

Throughout the pressure measurement range, the frequency (squared and averaged in the splitting) of the E2 line fits in the linear dependence

$$\frac{\omega_1^2 + \omega_2^2}{2} = 568^2 + 4.97 \times 10^3 P\,, \tag{78}$$

plotted in Fig. 23a, where the frequency is taken in cm^{-1} and the pressure in GPa.

However, for the A1 mode there are two linear portions — one at pressures below 20 GPa,

$$\omega_3^2 = 523^2 + 4.78 \times 10^3 P\,, \tag{79}$$

and the other above 23 GPa,

$$\omega_3^2 = 544^2 + 4.62 \times 10^3 P\,, \tag{80}$$

i.e., the frequency of this mode rises rather steeply in the transition from the metal to the semiconductor state.

The sharp change of the A1 line position at a pressure of about 20 GPa correlates with its narrowing shown in Fig. 23b. One can see that, aside from the contribution of scattering by defects to the widths of all lines, which increases with pressure, for the longitudinal A1 mode there is a significant contribution to the width only in the metal state. Therefore, the electronic nature of the transition in GaN under pressure is also confirmed by Raman scattering investigations.

7. Conclusion

In recent years, micro-Raman spectroscopy has been found to be a fine instrument which enables us to investigate the defect and stress distributions in semiconductors with a spatial resolution on the order of 1 μm. The mechanism of Raman line broadening, which invokes the quantum-mechanical theory of phonon scattering by defects, provides an explanation of the picture observed. At the same time, of special interest, both from the theoretical standpoint and for applications, is the possibility of measuring the electron – phonon interaction constant with the aid of Raman scattering or X-ray investigations. The most crude result of the presence of carriers reduces to the softening and broadening of phonons: this is the effect of Coulomb screening. The electron – phonon (deformation or Fröhlich) interaction arises due to the non-adiabaticity of the system of electrons and ions. We emphasize that this interaction yields a nonzero result only with the inclusion of anisotropy. Against the background of the screening, this interaction shows up as some small yet perfectly observable effect, which would be desirable to measure.

I take the opportunity to express my appreciation to E Mishchenko for his cooperation; J Camassel initiated the work, and I am particularly grateful to him for collaboration in the GES (Montpellier, CNRS). I would also like to express my gratitude to P Fulde (Dresden, MPIPKS) for his

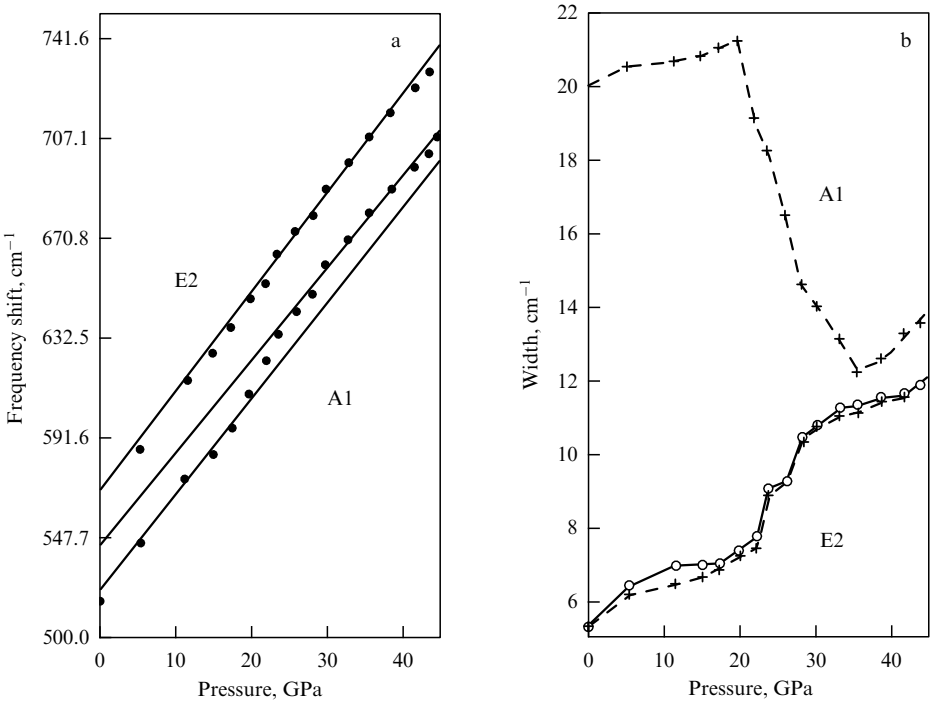

Figure 23. Variation of the frequency and width of the E2 and A1 resonances in GaN under pressure.

hospitality and the opportunity to complete this work, as well as to the Russian Foundation for Basic Research for its financial support.

References

1. Klemens P G *Phys. Rev.* **148** 845 (1966)
2. Debernardi A, Baroni S, Molinari E *Phys. Rev. Lett.* **75** 1819 (1995)
3. Barker A S (Jr), Sievers A J *Rev. Mod. Phys.* **47** (Suppl. 2) S1 (1975)
4. Taylor D W, in *Dynamical Properties of Solids* Vol. 2 *Crystalline Solids, Applications* (Eds G K Horton, A A Maradudin) (Amsterdam: North-Holland Publ. Co., 1975) p. 285
5. Klein M V, in *Dynamical Properties of Solids* Vol. 6 *The Modern Physics of Phonons* (Eds G K Horton, A A Maradudin) (Amsterdam: North-Holland Publ. Co., 1990) p. 65
6. Plekhanov V G *Usp. Fiz. Nauk* **173** 711 (2003) [*Phys. Usp.* **46** 689 (2003)]
7. Cardona M, Ruf T *Solid State Commun.* **117** 201 (2001)
8. Cerdeira F et al. *Phys. Rev. B* **5** 580 (1972)
9. Merle P et al. *Phys. Rev. B* **21** 1617 (1980)
10. Feng Z C, Choyke W J, Powell J A *J. Appl. Phys.* **64** 6827 (1988)
11. Weinstein B A, Zallen R, in *Light Scattering in Solids IV*: *Electronic Scattering, Spin Effects, SERS, and Morphic Effects* (Topics in Applied Physics, Vol. 54, Eds M Cardona, G Güntherodt) (Berlin: Springer-Verlag, 1984) p. 463
12. Yakovenko E V, Goncharov A F, Stishov S M *High Pressure Res.* **7** 433 (1991)
13. Ulrich C et al. *Phys. Rev. Lett.* **78** 1283 (1997)
14. Yakovenko E V, Gauthier M, Polian A *Zh. Eksp. Teor. Fiz.* (2004) (in press)
15. Tiong K K et al. *Appl. Phys. Lett.* **44** 122 (1984)
16. Richter H, Wang Z P, Ley L *Solid State Commun.* **39** 625 (1981)
17. Campbell I H, Fauchet P M *Solid State Commun.* **58** 739 (1986)
18. Tamura S *Phys. Rev. B* **30** 849 (1984)
19. Göbel A et al. *Phys. Rev. B* **59** 2749 (1999)
20. Ager J W III, Veirs D K, Rosenblatt G M *Phys. Rev. B* **43** 6491 (1991)
21. Wagner J et al. *Phys. Rev. B* **40** 1817 (1989)
22. Schwoerer-Böhning M, Macrander A T, Arms D A *Phys. Rev. Lett.* **80** 5572 (1998)
23. Falkovsky L A *Pis'ma Zh. Eksp. Teor. Fiz.* **66** 817 (1997) [*JETP Lett.* **66** 860 (1997)]
24. Camassel J, Contreras S, Robert J L *C.R. Acad. Sci. Ser. IV* **1** 5 (2000)
25. Falkovsky L A, Bluet J M, Camassel J *Phys. Rev. B* **55** R14697 (1997)
26. Falkovsky L A, Bluet J M, Camassel J *Phys. Rev. B* **57** 11283 (1998)
27. Cree Research Inc., http://cree.com/
28. Camassel J et al. *Electron. Lett.* **35** 1284 (1999)
29. Camassel J, Falkovsky L A, Planes N *Phys. Rev. B* **63** 035309 (2001)
30. "Silicon-on-insulator technology" *MRS Bulletin* **23** (12) (1998)
31. Tong Q-Y, Gösele U *Semiconductor Wafer Bonding*: *Science and Technology* (The Electrochemical Soc. Series) (New York: John Wiley, 1999)
32. Bruel M *Electron. Lett.* **58** 1284 (1999)
33. Letavic T J et al., in *Proc. of the 1st Intern. Symp. on Semiconductor Wafer Bonding*: *Science, Technology and Applications, Phoenix, Ariz., USA, 1991* (Proc. Electrochemical Soc., Vol. 92-7, Ed. U Gösele) (Pennington, NJ: Electrochemical Soc., 1992) p. 397
34. Schwarz K W *Phys. Rev. Lett.* **78** 4785 (1997)
35. Gillard V T, Nix W D, Freund L B *J. Appl. Phys.* **76** 7280 (1994)
36. Romanov A E et al. *J. Appl. Phys.* **85** 182 (1999)
37. Charpenay S et al., in *Proc. of the 1998 IEEE Intern. SOI Conf.* (1998) p. 43
38. Scott J F, Porto S P S *Phys. Rev.* **161** 903 (1967)
39. Kleinman D A, Spitzer W G *Phys. Rev.* **125** 16 (1962)
40. Jayaraman A, Wood D L, Maines R G (Sr) *Phys. Rev. B* **35** 8316 (1987)
41. Camassel J, Goullet A, Pascual J *Phys. Rev. B* **38** 8419 (1988)
42. Kirk C T *Phys. Rev. B* **38** 1255 (1988)
43. Kamitsos E I, Patsis A P, Kordas G *Phys. Rev. B* **48** 12499 (1993)
44. Lifshitz I M *Zh. Eksp. Teor. Fiz.* **17** 1017 (1947); *Nuovo Cimento* **3** (Suppl.) 716 (1956); *Usp. Fiz. Nauk* **83** 617 (1964) [*Sov. Phys. Usp.* **7** 549 (1965)]
45. Böttger H *Principles of the Theory of Lattice Dynamics* (Weinheim: Physik-Verlag, 1983) Ch. 2
46. Lifshits I M, Gredeskul S A, Pastur L A *Introduction to the Theory of Disordered Systems* (New York: Wiley, 1988)
47. Rohmfeld S, Hundhausen M, Ley L *Phys. Rev. B* **58** 9858 (1998)
48. Nakashima S et al. *Appl. Phys. Lett.* **77** 3612 (2000)
49. Falkovsky L A *Phys. Rev. B* **64** 024301 (2001)

50. Born M, Huang K *Dynamical Theory of Crystal Lattices* (Oxford: Clarendon Press, 1954) [Translated into Russian (Moscow: IL, 1958) Ch. 2, 5]
51. Vaks V G *Vvedenie v Mikroskopicheskuyu Teoriyu Segnetoelektrikov* (Introduction to the Microscopic Theory of Ferroelectrics) (Moscow: Nauka, 1973) Ch. 6
52. Grille H, Schnittler Ch, Bechstedt F *Phys. Rev. B* **61** 6091 (2000)
53. Bungaro C, Rapcewicz K, Bernholc J *Phys. Rev. B* **61** 6720 (2000)
54. Falkovsky L A *Zh. Eksp. Teor. Fiz.* **119** 966 (2001) [*JETP* **92** 840 (2001)]
55. Feldman D W et al. *Phys. Rev.* **170** 698 (1968); **173** 787 (1968)
56. Fal'kovskiĭ L A, Camassel J *Pis'ma Zh. Eksp. Teor. Fiz.* **69** 247 (1999) [*JETP Lett.* **69** 268 (1999)]
57. Loudon R *Adv. Phys.* **13** 423 (1964)
58. Harima H, Nakashima S, Uemura T *J. Appl. Phys.* **78** 1996 (1995)
59. Olego D, Cardona M *Phys. Rev. B* **23** 6592 (1981)
60. Feldman D W, Parker J H (Jr), Ashkin M *Phys. Rev. Lett.* **21** 607 (1968)
61. Bolotin G A, Ponosov Yu S *Fiz. Tverd. Tela* **27** 2636 (1985); **30** 986 (1988) [*Sov. Phys. Solid State* **27** 1581 (1985); **30** 572 (1988)]
62. Cardona M, Ipatova I P, in *Elementary Excitations in Solids* (Eds J L Birman, C Sébenne, R F Wallis) (Amsterdam: North-Holland, 1992) Ch. 13, p. 264
63. d'Astuto M et al. *Phys. Rev. Lett.* **88** 167002 (2002); cond-mat/0201501
64. Migdal A B *Zh. Eksp. Teor. Fiz.* **34** 1438 (1958) [*Sov. Phys. JETP* **7** 996 (1958)]
65. Abrikosov A A, Gor'kov L P, Dzyaloshinskiĭ I E *Metody Kvantovoĭ Teorii Polya v Statisticheskoĭ Fizike* (Methods of Quantum Field Theory in Statistical Physics) 2nd ed. (Moscow: Dobrosvet, 1998) p. 277 [Translated into English: *Quantum Field Theoretical Methods in Statistical Physics* 1st ed. (Oxford: Pergamon Press, 1965)]
66. Brovman E G, Kagan Yu *Zh. Eksp. Teor. Fiz.* **52** 557 (1967) [*Sov. Phys. JETP* **25** 365 (1967)]
67. Kontorovich V M *Usp. Fiz. Nauk* **142** 265 (1984) [*Sov. Phys. Usp.* **27** 134 (1984)]
68. Engelsberg S, Schrieffer J R *Phys. Rev.* **131** 993 (1963)
69. Alexandrov A S, Schrieffer J R *Phys. Rev. B* **56** 13731 (1997)
70. Maksimov E G, Shulga S V *Solid State Commun.* **97** 553 (1996)
71. Reizer M *Phys. Rev. B* **61** 40 (2000)
72. Gurevich V L, Larkin A I, Firsov Yu A *Fiz. Tverd. Tela* **4** 185 (1962) [*Sov. Phys. Solid State* **4** 131 (1962)]
73. Ipatova I P, Subashiev A V *Zh. Eksp. Teor. Fiz.* **66** 722 (1974) [*Sov. Phys. JETP* **39** 349 (1974)]
74. Ponosov Yu S et al. *Phys. Status Solidi B* **208** 257 (1998)
75. Abstreiter G, Cardona M, Pinczuk A *Light Scattering in Solids IV: Electronic Scattering, Spin Effects, SERS, and Morphic Effects* (Topics in Applied Physics, Vol. 54, Eds M Cardona, G Güntherodt) (Berlin: Springer-Verlag, 1984) p. 5
76. Falkovsky L A *Zh. Eksp. Teor. Fiz.* **124** 886 (2003) [*JETP* **97** 794 (2003)]
77. Mermin N D *Phys. Rev. B* **1** 2362 (1970)
78. Falkovsky L A, Mishchenko E G *Phys. Rev. B* **51** 7239 (1995)
79. Falkovsky L A, Klama S *Physica C* **264** 1 (1996)
80. Falkovsky L A *Phys. Rev. B* **66** 020302(R) (2002); *Zh. Eksp. Teor. Fiz.* **122** 411 (2002) [*JETP* **95** 354 (2002)]
81. Landau L D, Lifshitz E M *Fizicheskaya Kinetika* (Physical Kinetics) (Moscow: Fizmatlit, 2001) [Translated into English (Oxford: Pergamon Press, 1981)]
82. Gantmakher V F, Levinson I B *Rasseyanie Nositeleĭ Toka v Metallakh i Poluprovodnikakh* (Scattering of Current Carriers in Metals and Semiconductors) (Moscow: Nauka, 1984) [Translated into English: *Carrier Scattering in Metals and Semiconductors* (Amsterdam: North-Holland, 1987)]
83. Abrikosov A A, Falkovsky L A *Zh. Eksp. Teor. Fiz.* **40** 262 (1961) [*Sov. Phys. JETP* **13** 179 (1961)]
84. Abrikosov A A, Genkin V M *Zh. Eksp. Teor. Fiz.* **65** 842 (1974) [*Sov. Phys. JETP* **38** 417 (1974)]
85. Zawadowski A, Cardona M *Phys. Rev. B* **42** 10732 (1990)
86. Fano U *Phys. Rev.* **124** 1866 (1961)
87. Hon D T, Faust W L *Appl. Phys.* **1** 241 (1973)
88. Artús L et al. *Phys. Rev. B* **60** 5456 (1999)
89. Fukasawa R, Perkowitz S *Phys. Rev. B* **50** 14119 (1994)
90. Perlin P et al. *Phys. Rev. B* **45** 83 (1992)
91. Perlin P et al. *Phys. Status Solidi B* **198** 223 (1996)
92. Falkovsky L A et al. *Phys. Rev. B* **57** 11349 (1998)